

## **Sensitivity Analysis for Characterizing the Impact of HNGD Model on the Prediction of Hydrogen Redistribution in Zircaloy cladding using BISON code**

Seok Bin Seo<sup>1</sup>, Edward M. Duchnowski<sup>1</sup>, Arthur T. Motta<sup>2</sup>, Bruce F. Kammenzind<sup>3</sup>, Nicholas R. Brown<sup>1,\*</sup>

<sup>1</sup> University of Tennessee – Knoxville, Knoxville, TN, USA 37902

<sup>2</sup> Penn State University – University Park, PA, USA 16801

<sup>3</sup> Naval Nuclear Laboratory, Bettis Atomic Power Laboratory, Pittsburgh, PA, USA

\* Corresponding author: nbrown49@utk.edu

### **Abstract**

Hydrogen in zirconium cladding is able to precipitate into zirconium hydrides which impacts cladding integrity. The Hydride Nucleation-Growth-Dissolution (HNGD) model in the BISON code accounts for the precipitation and dissolution kinetics of hydride in Zircaloy material. This paper presents a global sensitivity analyses of the HNGD model aiming to enhance our understanding of the hydride precipitation phenomena by quantifying the variance that key parameters have on the prediction of hydrogen behavior under various environmental conditions. Model predictions are compared to experimental data obtained under two different conditions: 1) with uniformly precharged specimens subjected to a linear thermal gradient, and 2) specimens precharged with a cathodically applied hydride rim at one end of the sample and subjected to an asymmetric thermal gradient. The Sobol sensitivity analysis identifies the key

parameters in the HNGD model for both types of specimens. For linear temperature cases, the heat of transport dominates the accuracy of predictions when no precipitation occurs at the cold end, while Terminal Solid Solubility for Dissolution ( $TSS_D$ ) is the most important parameter when precipitation occurs. A large variation in the predicted hydrogen concentration profiles is found in the range of high  $TSS_D$  due to the occurrence of precipitation. For asymmetric temperature cases, the solubility coefficient gives the largest impact on the predicted hydrogen distribution, as it determines the amount of solute hydrogen dissolved from the initially applied hydride rim. A large discrepancy in hydrogen distribution between simulations and experiments exists with the asymmetric specimens because BISON simulations fail to predict the precipitation of hydride at the cooler end. Comparative studies using former and updated models verifies the significant impact of the hydride growth mechanism on predicted hydrogen concentration profiles. In particular, when hydride initially exists, changes in  $TSS_D$  generate a large variation in the predicted amount of precipitation by hydride growth, giving large uncertainty in predicting the hydrogen distribution over the sample length. The outputs characterize the significant impact of the hydride growth mechanism in the HNGD model on predicting hydrogen behavior, and improve the understanding of the precipitation of hydride in Zircaloy cladding within a range of expected environmental conditions. The analyses indicate work is still needed to improve the hydride solvus models in the BISON code to accurately predict experimentally observed hydride concentrations and distributions.

# Table of Contents

<b>Abstract .....</b>	<b>1</b>
<b>1. Introduction.....</b>	<b>4</b>
<b>2. Background .....</b>	<b>8</b>
2.1 Hydrogen diffusion in zirconium-based cladding.....	8
2.2 Precipitation and dissolution kinetics of hydrogen in zirconium-based cladding .....	10
2.3 Historical experiments.....	13
<b>3. Methodology.....</b>	<b>15</b>
3.1 Fuel performance code, BISON .....	15
3.2 Global sensitivity technique, Sobol .....	16
<b>4. Results and Discussion .....</b>	<b>18</b>
4.1 Global sensitivity analysis of the HNGD model under a linear temperature profile .....	18
4.2 Global sensitivity analysis of the HNGD model under asymmetric temperature profiles .....	34
4.3 Comparison study between the former BISON model and the HNGD model.....	41
4.3.1 Comparison study for linear temperature case .....	42
4.3.2 Comparison study for asymmetric temperature case.....	46
<b>5. Conclusion .....</b>	<b>48</b>
<b>Acknowledgement.....</b>	<b>50</b>
<b>REFERENCES .....</b>	<b>51</b>

# 1. Introduction

Zirconium alloys are used as cladding in Light Water Reactors (LWRs) to encase the nuclear fuel and act as the primary defense of fission product release into the environment. Zirconium has many attractive properties from a nuclear materials standpoint that make it a top contender for nuclear cladding. The low cross-section for thermal neutrons associated with zirconium as well as its resistance to corrosion in high temperature water within a nuclear reactor core make it a desired material to be utilized (A. Tanweer, et al., 2011). However, zirconium still experiences some corrosion during normal operation of an LWR while in contact with the water coolant/moderator. This forms a zirconium oxide layer on the outer surface of the cladding and allows a fraction of the freed hydrogen to ingress into the cladding (Motta A. T., et al, 2019). Hydrogen, having a high diffusivity in zirconium, is able to redistribute in the cladding and may precipitate into zirconium hydrides if the local concentration of hydrogen in solid solution exceeds the solubility limit (Ells C. E., 1968). This precipitation of hydrides leads to embrittlement and can lead to cladding failure (Arsene S., et al, 2003), which is of primary concern during nuclear reactor operation as well as spent fuel transportation and storage.

To account for hydride formation throughout the cladding, previous work implemented a hydrogen predictive model into the fuel performance code, BISON (Courty, O. et al, 2014) and succeeded in presenting the sequential phenomena (Stafford, 2015). More recent studies introduced several new findings to the predictive model in BISON and validated it with historic experiments (Lacroix E. et al., 2021) (Passelaigue F. et al., 2021). The new findings were implemented under the Hydride Nucleation-Growth-Dissolution (HNGD) BISON update. This paper presents a sensitivity and uncertainty analysis of the HNGD model to quantify the impact

of the improved model on the prediction of hydrogen behavior within the cladding. This includes identifying key parameters in the HNGD model under different environmental conditions, and revealing the significant impact of newly-implemented phenomena by comparison with the former BISON model. Sobol sensitivity calculations, which is the unique feature of this paper, are calculated to characterize the key input parameters involved in the model with regards to the predicted hydrogen distribution.

Several modeling and simulations of length-scales from nano to micro-scale as well as from atomic and mesoscale have been devoted to account for the precipitation kinetics of hydrides in zirconium-based materials. While atomic scale modeling has provided insights into hydrogen diffusion as well as crucial information on hydride properties, mesoscale methods are needed to describe the formation and growth of the nanoscale hydrides at sufficiently large length and time scales (Motta A. T., et al, 2019). The information obtained from atomistic and meso-scale modeling then helps inform and improve models of hydrogen behaviors at larger scales. Hamamoto et al. (Hamamoto, Uchikoshi, & Tanabe, 2020) developed kinetic models of hydrogen absorption for zirconium by describing hydrogen-transport processes and bulk diffusion, but the model did not consider the formation of hydrides. Bruni et al. (Bruni, Lewis, & Thompson, 2010) developed a kinetics model using the COMSOL multiphysics platform that accounts for hydrogen transport driven by a concentration gradient and a temperature gradient. In the simulation, a moving interface was present between a region that had hydride formation and a region without. To account for this, a moving mesh with an interface boundary velocity was applied using Arbitrary Lagrangian-Eularion formulation. Kolesnik et al (Kolesnik, Aliev, & Likhanskii, 2018) modeled hydride reorientation in spent fuel under dry storage conditions. The model assumed that hydride orientation was determined by hydride nucleus orientation. While

model parameters were validated with experiments, it was recommended that additional experimental and modeling studies of hydrogen redistribution kinetics were required.

Courty et al. (Courty, O. et al, 2014) implemented a hydrogen transport and distribution model in BISON that accounted for Fick's law, Soret effect, and hydride precipitation which occurred once the hydrogen solubility limit was reached. The implemented model predicted hydrogen accumulation near colder regions of the cladding due to the Soret effect and the temperature dependence on the solubility of hydrogen in solid solution in the zirconium cladding. The model predicts that reactor shutdowns had limited impact on hydride distribution. Stafford (Stafford, 2015) modeled hydrogen and hydride distribution in Zr cladding throughout the life cycle of a fuel rod with 2D simulations using the hydride model in BISON. The study predicted the formation of a hydride rim when spent fuel was stored under dry cask storage conditions, though the model had difficulties determining the hydride rim thickness. The former hydrogen migration and redistribution model in the BISON code predicts the formation of hydrides only when the concentration of hydrogen in solid solution exceeds the Terminal Solid Solubility for Precipitation ( $TSS_P$ ) and the dissolution of hydrides into hydrogen in solid solution when the concentration of hydrogen in solid solution is below the Terminal Solid Solubility for Dissolution ( $TSS_D$ ). The region in between the  $TSS_P$  and  $TSS_D$  limits is known as the hysteresis region where it was previously assumed that precipitation and dissolution do not occur. The HNGD model builds on studies that conclude that hydride concentration increases can occur in the hysteresis region by the growth of existing hydrides. Hydride concentration increases occur above  $TSS_P$  from both nucleation of new hydrides and the growth of existing hydrides (Lacroix E. et al., 2021). A recent study by Passelaigue et al. (Passelaigue F. et al., 2021) implemented this improved understanding of hydride precipitation kinetics into the BISON code and validated

it with historical experiments showing improvement in predicted hydride precipitation relative to the former version.

The work presented here aims to enhance our understanding of the new hydrogen predictive model by quantifying the impact of various environmental conditions on the prediction of hydrogen behavior. This paper focuses on a sensitivity analysis to investigate the contributions of proposed precipitation and dissolution mechanisms to the prediction of hydrogen migration in the zirconium cladding using the HNGD model. Sensitivity analysis can help improve the accuracy of hydrogen predictive models by identifying key parameters and their effects on the predicted hydride formation and distribution. Zineb et al. (Aly Z., et al, 2019) (Aly Z., et al., 2019) verified and validated the former BISON model for hydrogen migration and redistribution, and developed a framework to quantify the impact of uncertainty of the physical parameters of the model. They focused on a limited set of data with uniformly precharged samples under linear temperature profiles, or samples cathodically precharged with a hydride rim on one end and subjected to asymmetric temperature profiles. Extended from these studies, Seo et al. (Seo, et al., 2021) conducted sensitivity analysis of the former BISON hydrogen transport model under linear temperature gradients to quantify impacts of the local conditions on the prediction and respective parameters involved in hydrogen migration and redistribution. The present paper studies both sets of experiments using the HNGD model and compares the results to those from the former version of the BISON model. Quantifying the impact of parameters is performed via a Sobol analysis technique which provides a ranking of importance for input parameters giving a Figure of Merit (FoM) output. The chosen FoMs was selected to be the relative Root Mean Square Error (RMSE) between the BISON predictions and the

experimentally measured hydrogen concentration which allows for examining the accuracy of the predicted hydrogen distribution along the entire sample.

The organization of the remainder of this paper is as follows. **Section 2** overviews the background of the HNGD model and historic experiments benchmarked for this study. **Section 3** describes the methodology used to model the hydrogen behaviors in the zirconium cladding and to analyze the impacts of input parameters on the prediction of hydrogen. **Section 4** presents sensitivity analysis of the HNGD model under various conditions from sets of historic experiments, and compares the sensitivity results of the HNGD model to the former BISON model. **Section 5** presents a summary and conclusions.

## **2. Background**

### *2.1 Hydrogen diffusion in zirconium-based cladding*

Hydrogen in solid solution in zirconium cladding is able to diffuse under three main phenomena, (i) concentration gradients of hydrogen in solid solution in the cladding due to Fick's law, (ii) thermal gradients in the cladding due to the Soret effect, and (iii) tensile and compressive stress gradients within the cladding (Courty, O. et al, 2014). The focus of hydrogen migration for this paper will be on Fick's law and the Soret effect, because the level of stress and stress gradient expected in our experiments where no external stress was applied is much lower than that required to affect hydrogen redistribution in Zr, such as occurs in delayed hydride cracking (Puls, 2012).

Both Fickian diffusion and the Soret effect influence the movement of hydrogen when it is in solid solution in zirconium. The equation used for the diffusion coefficient for hydrogen in solid solution in zirconium follows an Arrhenius relation as stated in Eq. (1).

$$D = D_0 \exp\left(-\frac{Q_D}{RT}\right) \quad (1)$$

where  $D_0$  is the diffusivity pre-exponential constant,  $Q_D$  is the activation energy,  $R$  is the universal gas constant, and  $T$  is the local temperature. The diffusion of hydrogen due to Fick's law is reliant on the local concentration of hydrogen in solid solution. Hydrogen will diffuse to lower solid solution concentrations until an equilibrium is reached within the median. The hydrogen flux in solid solution as it relates to Fickian diffusion is given by:

$$J_{Fick} = -D\nabla C_{ss} \quad (2)$$

where  $D$  is the diffusion constant from Eq. (1), and  $\nabla C_{ss}$  is the local concentration gradient of hydrogen in solid solution within the zirconium cladding.

The Soret effect is driven by the temperature gradient within a sample. Hydrogen in solid solution will migrate from higher temperatures to lower temperatures. The equation for hydrogen flux in solid solution as it relates to the Soret Effect is stated in Eq. (3).

$$J_{Soret} = -\frac{DC_{ss}Q^*}{RT^2}\nabla T \quad (3)$$

where  $C_{ss}$  is the local concentration of hydrogen in solid solution,  $Q^*$  is the heat of transport and  $\nabla T$  is the local temperature gradient. Combining Equations 2 and 3, hydrogen migration in solid solution in the zirconium lattice, driven by both solid solution concentration gradients and temperature gradients is described by:

$$J = -D\nabla C_{ss} - \frac{DC_{ss}Q^*}{RT^2}\nabla T \quad (4)$$

Note that hydrogen migration model in BISON code neglects diffusion of hydrogen in the hydride ( $\delta$ -phase), and only the migration of hydrogen in solid solution in the zirconium lattice is modelled (see Eq. (2)), as the migration of hydrogen through the zirconium hydride phase is orders of magnitude slower (Stafford, 2015). The zirconium hydride phase is treated only as a source or a sink for hydrogen into or out of solid solution.

## *2.2 Precipitation and dissolution kinetics of hydrogen in zirconium-based cladding*

Once the hydrogen solid solution concentration reaches solubility in the alloy, the zirconium hydride phase begins to precipitate out of solution. Hydrogen precipitation from solid solution into hydrides, or dissolution from hydrides into solid solution is a function of both the local concentration of hydrogen and temperature. The volume fraction of hydrides formed depends on the total concentration of hydrogen in the alloy as well as the alloy's terminal solid solubilities for precipitation ( $TSS_P$ ) and for dissolution ( $TSS_D$ ).  $TSS_P$  and  $TSS_D$  represent the precipitation and dissolution limits, respectively, and are described using the Arrhenius formulas:

$$TSS_P = TSS_{P0} \exp\left(-\frac{E_P}{RT}\right) \quad (5)$$

$$TSS_D = TSS_{D0} \exp\left(-\frac{E_D}{RT}\right) \quad (6)$$

where  $TSS_{P0}$  and  $TSS_{D0}$  are pre-exponential factors with units of wt.ppm,  $E_P$  and  $E_D$  are the activation energies in J/mol for  $TSS_P$  and  $TSS_D$ , respectively.

The former version of the BISON model describes the rate of precipitation and dissolution,  $S$ , as a kinetic equation, Eq. (7), where the constants are determined empirically and follow an Arrhenius law, as shown in Eqs. (8) and (9), respectively. The piece-wise function in Eq. (7) describes the hysteresis between the dissolution and the precipitation solvus, where precipitation of hydrogen in solid solution occurs if the concentration is greater than  $TSS_P$ , and dissolution of existing hydride occurs if the concentration of hydrogen in solid solution is less than  $TSS_D$ . When the concentration of hydrogen in solid solution is greater than  $TSS_D$  but less than  $TSS_P$ , no precipitation or dissolution occurs.

$$S = \left\{ \begin{array}{ll} \alpha^2(C_{SS} - TSS_P) & \text{if } TSS_P < C_{SS} \\ 0 & \text{if } TSS_D < C_{SS} < TSS_P \\ \beta^2(C_{SS} - TSS_D) & \text{if } C_{SS} < TSS_D \end{array} \right\} \quad (7)$$

$$\alpha = A_\alpha \exp\left(\frac{E_\alpha}{RT}\right) \quad (8)$$

$$\beta = A_\beta \exp\left(\frac{E_\beta}{RT}\right) \quad (9)$$

where  $A_\alpha$  and  $A_\beta$  are the pre-exponential factors for the precipitation and dissolution kinetic parameters, respectively.  $E_\alpha$  and  $E_\beta$  are the activation energies for the precipitation and dissolution kinetic parameters, respectively. In the original BISON model implemented into the code by Stafford (Stafford, 2015), dissolution kinetics is taken as instantaneous in relation to the rate at which hydrogen can diffuse in solid solution.

The HNGD model divides the mechanisms of hydride precipitation into nucleation of new hydrides and growth of existing ones. The nucleation of new hydrides only occurs when the hydrogen content in solid solution is above the supersolubility limit (equivalent to  $TSS_P$ ), while the growth of existing hydrides occurs when the hydrogen content in solid solution is above  $TSS_D$  which is identified as the thermodynamic solubility limit (Lacroix, Motta, & Almer, 2018). The dissolution of hydrides happens below  $TSS_D$  and is no longer considered instantaneous. Each mechanism has its own kinetic parameter defined in Eqs. (10)-(12). Note that the growth of hydrides is limited by two factors, diffusion (subscript ‘mob’) and the reaction rate at the hydride matrix interface (subscript ‘th’ for thermodynamics). Both of these limitations are incorporated into the overall growth kinetic parameter,  $K_G$ . A description of the new kinetic parameters is as follows:

$$\text{Dissolution: } K_D = K_{D0} \exp\left(-\frac{E_D}{RT}\right) \quad (10)$$

$$\text{Nucleation: } K_N = K_{N0} \exp\left(-\frac{E_{th}}{RT}\right) \quad (11)$$

$$\text{Growth: } K_G = \left(\frac{1}{K_{mob}} + \frac{1}{K_{th}}\right)^{-1} \left\{ \begin{array}{l} \text{Diffusion Controlled: } K_{mob} = K_{mob0} f_\alpha v_0 \exp\left(-\frac{E_G}{RT}\right) \\ \text{Reaction Controlled: } K_{th} = K_{th0} f_\alpha v_0 \exp\left(-\frac{E_{th}}{RT}\right) \end{array} \right\} \quad (12)$$

where  $K_{D0}$ ,  $K_{N0}$ ,  $K_{mob0}$ , and  $K_{th0}$  are the pre-exponential factors for dissolution, nucleation, diffusion-controlled growth, and reaction-controlled growth, respectively.

The respective mechanisms occur at their specific rates (equivalent to  $S$ ) determined by kinetic parameters, as given by:

$$\text{Dissolution: } \frac{\delta C_{SS}}{\delta t} = -K_D(C_{SS} - TSS_D) \quad (13)$$

$$\text{Nucleation: } \frac{\delta C_{SS}}{\delta t} = -K_N(C_{SS} - TSS_P) \quad (14)$$

$$\text{Growth: } \frac{\delta C_{SS}}{\delta t} = -K_G(C_{tot} - TSS_D)p(1-x)(-\ln(1-x))^{1-\frac{1}{p}} \quad (15)$$

Finally, the differential equations for the evolution of hydrogen concentration in solid solution and for the evolution of the volume fraction of  $\delta$ -ZrH<sub>1.66</sub>,  $V_\delta$  are given by a balance equation for hydrogen in solid solution and hydride concentration (Stafford, 2015), as follows:

$$\frac{\partial V_\alpha C_{SS}}{\partial t} = -\nabla \cdot V_\alpha J_{tot} - V_\alpha S, \text{ where } V_\alpha \equiv 1 - V_\delta \quad (16)$$

$$\frac{\partial V_\delta}{\partial t} = \frac{M_{ZrH_{1.66}}}{M_H} \frac{V_\alpha S}{1.66} \quad (17)$$

where  $V_\alpha$  is the volume fraction of the  $\alpha$ -Zr phase.

### *2.3 Historical experiments*

The experiments of hydrogen diffusion and precipitation discussed in this paper were conducted by Kammenzind et al. to examine hydrogen migration in unirradiated alpha-annealed Zircoloy-4 under various conditions (Kammenzind B. F., et al., 1996) and reviewed in a Masters thesis at Penn State University (Merlino J. T., 2019). The experiments were divided into two sets, linear temperature profiles and asymmetric temperature profiles. The asymmetric temperature profile specimens of 3.81 cm long, 1.27 cm wide, and 0.127 cm thick, have a small amount of hydride initially present in the majority of the sample (10 ppm) with a solid hydride rim located at the hotter end of the sample. Each specimen's hydride rim was about 75 micrometers thick, coating approximately the last one millimeter of the hotter end of the specimen. The significance of an initially charged hydride rim is that hydrogen is not evenly distributed within the zirconium cladding during normal operation because of the temperature profile within the cladding (Asher, R. C., and F. W. Trowse, 1970) which results in non-uniform radial distributions of hydrogen concentration as well as non-uniform axial distributions at the inter-pellet regions (Motta A. T., et al, 2019). The annealing temperature gradient for a series of experiments had a colder side temperature of either 260 °C or 316 °C, a peak temperature of 371 °C about 2.54 cm from the colder side, and a hotter side temperature at the other end of the specimen with a temperature between the colder side and the peak temperature. Asymmetric temperature profiles are also more prevalent in dry cast storage with vacuum or low fill gas density (Richmond D. J. and Geelhood K. J., 2018). These specimens were annealed for periods between 100 and 200 days.

The linear temperature profile experiments had a homogenous initial hydrogen loading throughout the 2.54 cm length, 1.27 cm width, and 0.127 cm thickness specimen. The differences in specimens within this set were the cold end temperature, temperature gradient, and annealing time, as well as the initial total hydrogen concentration. The temperature at the cold end of the specimens was set to either 260°C, 316°C, 371°C, or 427°C, and the temperature gradient was targeted at either 66°C/cm or 87°C/cm. The specimen was annealed for about ten to eighty days.

All sets of experiments started at room temperature and were then raised to their respective temperature profiles within a short time. The asymmetric temperature profiles were annealed for much longer times because of the longer diffusion distance, shallower thermal gradients, and overall lower temperatures in the samples. All the experiments were conducted in an air environment keeping an oxide surface film on the samples, preventing hydrogen egress from the samples. Following annealing, the specimens were brought to room temperature to fix the hydrogen distribution. The specimens were sectioned and the total hydrogen content was measured from each section. More on the experimental data and procedure can be found in (Kammenzind B. F., et al., 1996).

### **3. Methodology**

#### *3.1 Fuel performance code, BISON*

BISON is an engineering-scale fuel performance code based on the finite element method, which was developed at the Idaho National Laboratory (Williamson R. L., et al, 2012). The BISON code has been primarily used to solve for the thermal and mechanical behavior of fuel as well as heat transfer. A previous study has implemented a method for modeling hydrogen

redistribution and migration within the fuel element Zr alloy cladding (Courty, O. et al, 2014). The model is also able to capture the oxidation that occurs on the outer surface of the cladding due to waterside corrosion. The model has been used to model the lifecycle of fuel rods, and has been validated against historical experiments (Stafford, 2015). More recently, the HNGD model for hydride precipitation and dissolution was implemented into the BISON code and validated (Passelaigue F. et al., 2021).

Several assumptions were made to make the BISON code able to simulate the hydrogen behaviors in the historical experiments described in **Section 2.3**: the temperature gradient was linearly interpolated between thermocouples along the specimen length, the total amount of hydrogen in the specimen was kept constant, and the hydrogen migration was modeled in one dimension, independent of the width or thickness of the specimen. The 40 mesh elements used for the linear temperature cases and the 1000 mesh elements for the asymmetric temperature cases were split evenly throughout the geometry, respectively, and the calculations simulated the duration of the experimental anneals. At each time step, BISON computes the concentrations of soluble hydrogen and zirconium hydrides as well as the time derivatives of hydrogen in solid solution. Then the code uses kernels and material properties to evaluate integral values associated with equations in **Section 2.2**, and computes final hydrogen concentration at each mesh point along the sample.

### *3.2 Global sensitivity technique, Sobol*

To quantify the uncertainty that BISON has on predicting the total posttest measured hydrogen content at the cold region of the sample, a global sensitivity study was performed on

each simulation. The approach used was a variance-based sensitivity analysis utilizing the Sobol sensitivity technique. This method was selected as it provides a more general approach to quantifying uncertainty as it allows for high dimensional input space and is not constrained to purely linear correlations, such as in a Pearson correlation (Sobol I., 1993) (Saltelli A. et al., 2010) (Saltelli A., 2002). The Sobol indices are given as either a first order effect or a total effect, Eq. (18) and Eq. (19) respectively. The first order effect represents the fraction of the variance with respect to a single input, and the total effect captures the first order effect as well as interactions with all other input parameters. To ensure that the Sobol indices have converged it was concluded that a confidence interval below 0.05 ensures convergence (Sarrazin F. et al., 2016). The method for performing this study was conducted utilizing the Python library SALib (Herman J. and Usher W, 2017) that performs the generating of variable inputs as well as the Sobol analysis. Coupling SALib with BISON used a fairly straightforward method, SALib would generate  $N * (2D + 2)$  BISON input decks, where  $N$  is the specified sample number and  $D$  is the number of parameters, each with a unique combination of variable inputs. Finally, after all cases have ran SALib would be used to parse the output of each case and perform the Sobol analysis for a target FoM.

$$S_{1st} = \frac{V_{X_i}(E_{X_{\sim i}}(f(X)|X_i))}{V(f(X))} \quad (18)$$

$$S_{Total} = \frac{E_{X_{\sim i}}(V_{X_i}(f(X)|X_{\sim i}))}{V(f(X))} \quad (19)$$

where  $S_{1st}$  and  $S_{Total}$  are the Sobol indices first order effect and total effect, respectively.  $V(f(X))$  is the variance of  $f(X)$ ,  $E_{X_{\sim i}}(f(X)|X_i)$  is the expected value of  $f(X)$  conditioned on  $X_i$ , and  $X_{\sim i}$  is the set of all inputs except  $X_i$ .

This paper interprets the results of the sensitivity analyses in two ways. A Sobol index calculated for each specimen indicates the relative importance of input parameters in impacting the FoM. This allows the identification of the dominant parameter as well as the phenomena involved in it when predicting the hydrogen behaviors in the specimen. The FoMs predicted by BISON using different combinations of input parameters are plotted with respect to a chosen parameter. This enables visualization of the relationship between outputs and respective inputs. Note that only the scatter plot of the most dominant parameter given by Sobol indices is presented for each specimen to avoid any redundant descriptions. The scatter plot may present different values of the FoM at the same value of a chosen parameter, because different combinations of other parameters produce different results.

## **4. Results and Discussion**

### *4.1 Global sensitivity analysis of the HNGD model under a linear temperature profile*

A Sobol sensitivity analysis of the HNGD model under linear temperature profiles was conducted with respect to an integrated set of input parameters. A key FoM in this study was the relative RMSE calculated for the predicted hydrogen concentration at different positions in the sample compared to the experimental data in (Merlino J. T., 2019), defined as:

$$relative\ RMSE = \frac{1}{C_{ini}} \sqrt{\frac{\sum_{i=1}^M (Y_{i,exp} - Y_{i,pre})^2}{M}} \quad (20)$$

where  $C_{ini}$  is the initially charged total hydrogen concentration for each case,  $Y_{i,exp}$  is the experimentally measured hydrogen concentration at the  $i$ -th point,  $Y_{i,pre}$  is the predicted total hydrogen concentration by BISON simulation at the  $i$ -th point, and  $M$  is the number of sections in the sample where the posttest hydrogen content was measured in the experiments. Note that  $Y_{pre}$  for each section is the averaged value over the finite volume of each posttest measurement section in order to compare with measured value.

The input parameters can be divided into thermodynamic quantities (e.g.,  $Q^*$ ,  $TSS_P$ , and  $TSS_D$ ) or kinetic parameters (e.g.,  $K_G$ ,  $K_D$ ,  $K_N$ , and  $D$ ). The default values of the parameters came from the original development of the HNGD model (Lacroix, Motta, & Almer, 2018) (Lacroix E. et al., 2021) and were hard wired into the BISON code (Passelaigue F. et al., 2021). A range of variation for each parameter was set to approximately span experimental values reported from previous studies. The heat of transport was varied by  $\pm 30\%$  from the default value so that the overall value was within a certain number of experimental values in (Kammenzind B. F., et al., 1996). We varied the pre-exponential factor of the diffusion coefficient by  $\pm 20\%$  from the measured value in (Kammenzind B. F., et al., 1996). The ranges of coefficients for supersolubility (=TSS<sub>P</sub>) and solubility (=TSS<sub>D</sub>) were set to  $\pm 15\%$  from their respective values which were calculated from an average fit of measured values in different sources (McMinn, Darby, & Schofield, 2000) (Une & Ishimoto, 2003) (Colas, Motta, Daymond, & Almer, 2014). Lastly, the input variables for the kinetic parameters were varied about  $\pm 5\%$  from the measured value reported in (Lacroix E. et al., 2021). Note that, for the Arrhenius law parameters ( $D$ ,  $TSS_P$ ,  $TSS_D$ ,  $K_N$ ,  $K_{mob}$ ,  $K_{th}$ , and  $K_D$ ), we varied pre-exponential factors while keeping the activation

energy constant, which allowed us to effectively vary the overall value by a certain range. And also, the variation ranges were determined to not exceed any of uncertainties in measurements within the temperature range reported in the sources. The input parameters and their respective ranges are listed in Table 1.

Table 1. Variation ranges for the major input parameters of HNGD model.

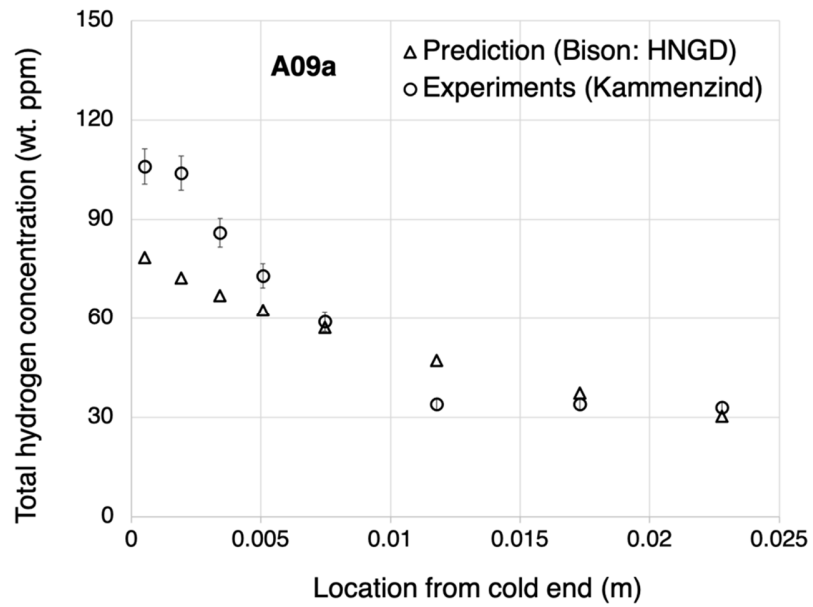
Parameter	Unit	Lower bound	Upper bound
Heat of transport, $Q^*$	<i>J/mole</i>	18200	33800
Diffusion coefficient: pre-exponential factor, $D_0$	<i>m<sup>2</sup>/s</i>	$6.3 \cdot 10^{-7}$	$9.5 \cdot 10^{-7}$
Supersolubility coefficient (=TSS <sub>P</sub> ), $TSS_{P0}$	<i>wt. ppm</i>	26350	35560
Solubility coefficient (=TSS <sub>D</sub> ), $TSS_{D0}$	<i>wt. ppm</i>	86700	117300
Nucleation kinetic parameter: coefficient, $K_{N0}$	<i>s<sup>-1</sup></i>	$2.6 \cdot 10^{-5}$	$2.9 \cdot 10^{-5}$
Diffusion-controlled growth kinetic parameter: coefficient, $K_{mob0}$	<i>s<sup>-1</sup></i>	52250	57750
Reaction-controlled growth kinetic parameter: coefficient, $K_{th0}$	<i>s<sup>-1</sup></i>	$1.52 \cdot 10^{-5}$	$1.68 \cdot 10^{-5}$
Dissolution kinetic parameter: coefficient, $K_{D0}$	<i>s<sup>-1</sup></i>	3900	4300

Sensitivity analyses of the key parameters involved in the HNGD model were conducted under the linear temperature gradient conditions using five different Zircaloy-4 specimens. Five specimens with different temperature profiles and initial hydrogen content were chosen from Kammenzind experiments (Kammenzind B. F., et al., 1996), as listed in Table 2. Note that these experiments were under a constant temperature gradient during the annealing phase and the hydrogen was initially distributed uniformly along the length of the specimen.

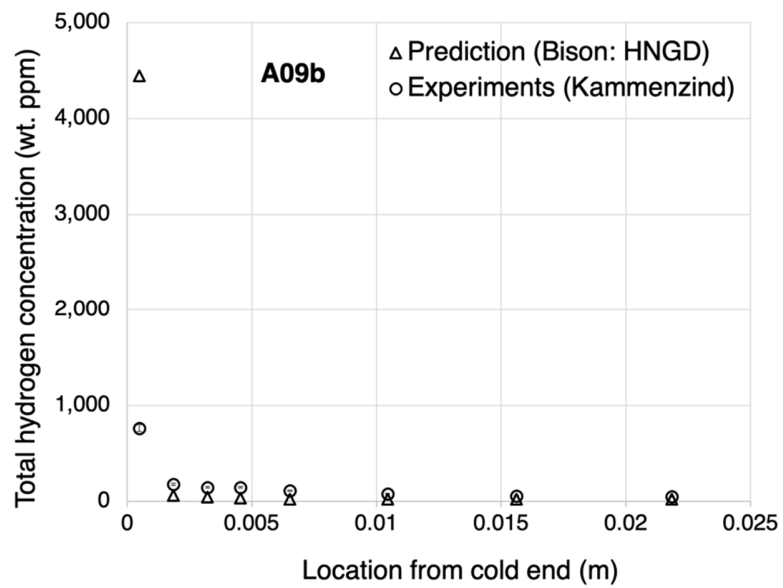
Table 2. Chosen experiments under linear temperature profile from historic data (Kammenzind B. F., et al., 1996)

	<b>Cold end Temp. [K]</b>	<b>Temp. gradient [K/cm]</b>	<b>Hot end Temp. [K]</b>	<b>Initial hydrogen content [wt.ppm]</b>	<b>Annealing time (day)</b>
A46	533	65.8	700	101	77
A09a	589	65.4	755	48	15
A09b	589	65.4	755	108	32
A12a	644	65.8	811	199	9
A14	700	76.4	894	261	6

BISON simulations using the hard-coded values for the parameters involved in the HNGD model represented two distinct results. In the case where no precipitation occurred at the cold end, like specimen A09a, the BISON code somewhat underpredicted the total hydrogen concentration along the length of the sample at the colder end as shown in Figure 1(a). On the other hand, the BISON code significantly overpredicted the total hydrogen distribution at the colder end when precipitation occurred, which caused a significant discrepancy between the predicted and measured hydrogen concentration (See Figure 1(b)). The results indicate that the current BISON code has considerable uncertainty in predicting the amount of hydride precipitation occurring at the cold end with respect to the posttest measured concentrations.



(a)



(b)

Figure 1. Chosen example of hydrogen distribution predicted from BISON code using default values: (a) case where no precipitation occurs at the cold end, (b) case where hydrides precipitate at the cold end.

Sobol indices computed for specimen A09a, as shown in Figure 2, indicate that the heat of transport had the largest influence for the conditions of this specimen where no precipitation of hydride occurred at the cold end by the end of the test period. This is because hydrogen diffusion in solid solution is the only phenomena involved in hydrogen migration when no precipitation occurs. The final measured profile is the results of both Fickian and Soret driven hydrogen migration, and the anneal times for this specimen were chosen to allow a steady state, time independent solid solution profile to develop.

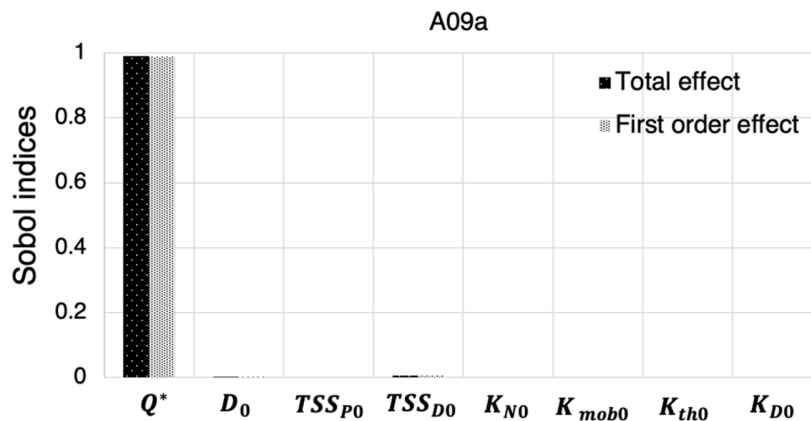
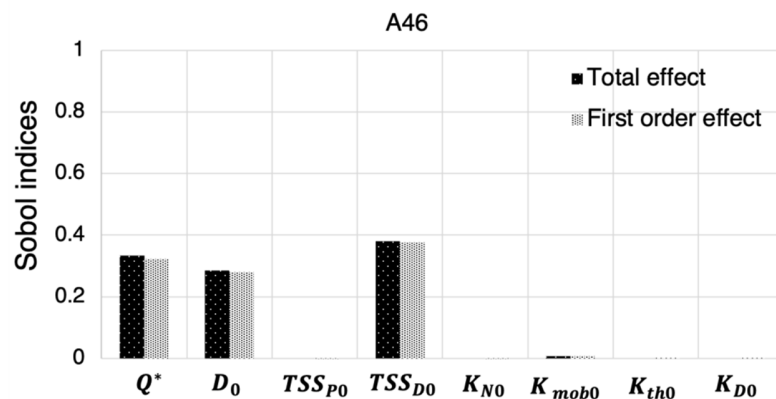


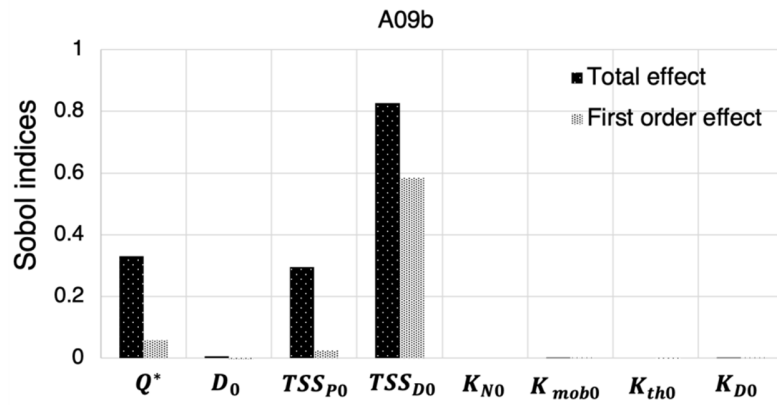
Figure 2. Sobol indices of relative RMSE computed for specimen A09a.

Figure 3(a)-(d) present Sobol indices calculated for the other specimens, three of which had hydride precipitated at the cold end by the end of the test period. For those cases, parameters involved in the precipitation and dissolution phenomena gave significant effects on the predicted hydrogen distribution. This indicates that once precipitation of hydride is predicted to occur at the cold end, the solid solution diffusion phenomenon no longer dominates the prediction of the final hydrogen concentration profile and the precipitation/dissolution phenomena become key. Furthermore, different Sobol indices under different experimental cases revealed high correlation

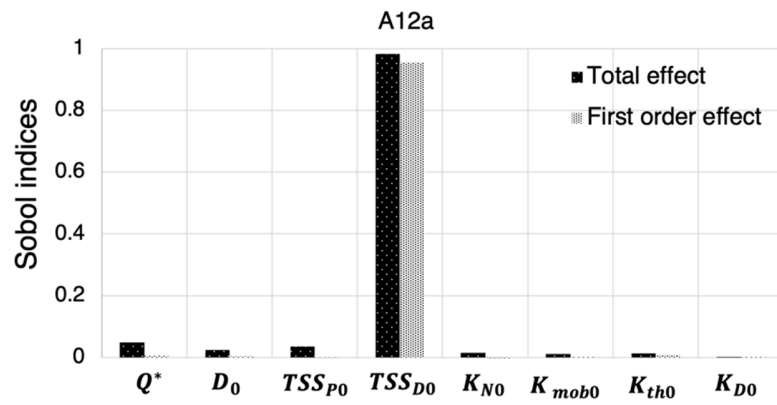
of the prediction accuracy to the specimen temperature profile and initial conditions. Generally, the contribution of  $TSS_D$  to the prediction of hydrogen distribution increased as the temperature at the cold end increased. However, at very high temperatures like in specimen A14,  $TSS_D$  did not provide any significant effect on the accuracy of the prediction, whereas the contribution of  $TSS_P$  among the parameters involved in the HNGD model largely increased. Given the fact that  $TSS_D$  and  $TSS_P$  are involved in the growth and dissolution of hydride, and the nucleation of hydride, respectively, it is inferred that the most influencing mechanism in the HNGD model changes from the growth/dissolution of hydrides to the nucleation of hydride as the temperature increased and as the amount of precipitated hydride at the cold end of the specimen at the start of testing decreased.



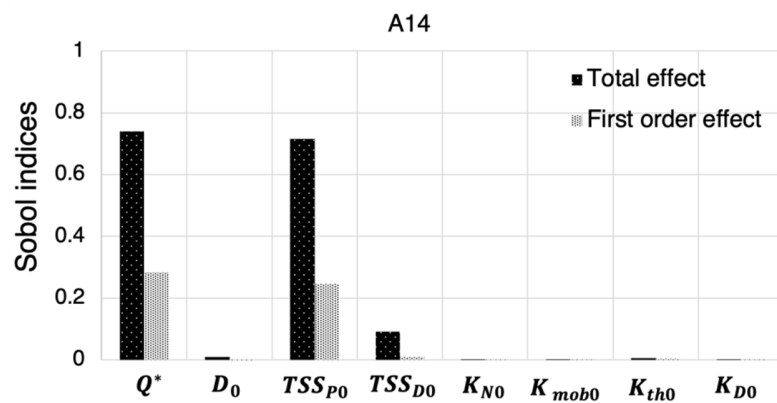
(a)



(b)



(c)



(d)

Figure 3. Sobol indices of key parameters involved in the HNGD model computed for each specimen: (a) A46, (b) A09b, (c) A12a, (d) A14.

Figure 4 presents the scatter plot of the computed relative RMSE with respect to the  $TSS_D$  coefficient for specimen A46. Note that hydrides precipitated at the cold end in all BISON simulations for specimen A46. The scatter plot indicates larger  $TSS_D$  values reduce the overall accuracy of the predicted hydrogen distribution. Since the largest error in prediction came from the overprediction of hydrogen at the cold end where hydrides precipitated (similar to Figure 1(b)), it is inferred that increasing  $TSS_D$  caused more precipitation of hydride. This is because higher  $TSS_D$  drove more diffusion to the cold end with a resulting larger concentration of precipitated hydrides. When the linear temperature profile was applied, hydrides at the hot end were initially dissolved and hydrogen migrated towards the cold end in the form of hydrogen in solid solution. Hydrides precipitated when the concentration of hydrogen in solid solution reached  $TSS_P$  creating a localized increase in hydride concentration, and continuous diffusion by Soret effect led to deficit of solute hydrogen. The localized increase in hydride concentration then dissolved again and the hydrogen reprecipitated further towards the cold end, forming a larger hydride concentration. This dissolution and precipitation cycle repeated during the whole experiment. Thus, the higher solubility was, the larger driving force for dissolution became, which accelerated the cycle and resulted in more hydrides to precipitate at the cold end.

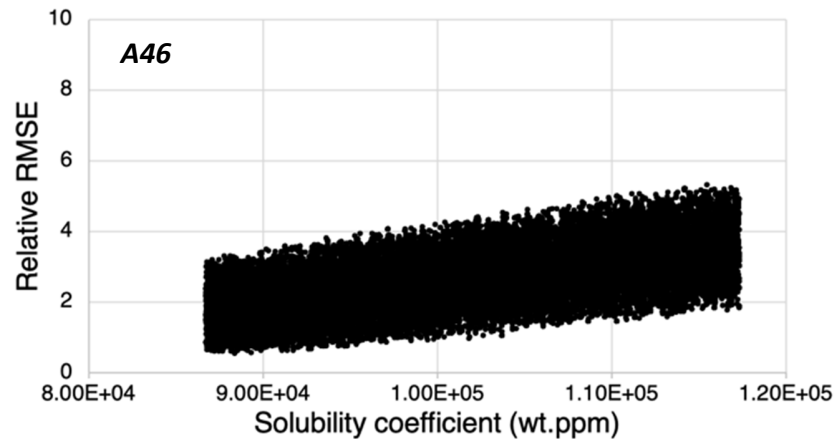


Figure 4. Scatter plot of relative RMSE with respect to the solubility coefficient for specimen A46.

Figure 5 presents the scatter plot of the computed relative RMSE with respect to the solubility coefficient for specimen A09b. As seen in the plot, there is large jump in the predicted RMSE in the higher range of the solubility coefficient. Note that the upper region is where precipitation is predicted to occur, and the bottom region is where there is no precipitation predicted to occur. Although hydrides precipitated at the cold end in the experiment for specimen A09b, the lowest RMSE was calculated from the BISON runs where there was no precipitation predicted. This is because, once precipitation is predicted to occur, the predicted hydrogen concentration drastically increased at the cold end due to a large amount of hydride precipitated. As a result, the difference to the hydrogen concentration measured from the posttest examination became much larger, reducing overall accuracy of the simulation, even lower than that calculated for no-precipitation runs. The same trend was observed from the scatter plot for specimen A12a, as shown in Figure 6.

The scatter plots in Figures 5 and 6 can be divided into four regions: (1) low RMSE values in the lower range of  $TSS_D$ , (2) increasing RMSE values in the midrange of  $TSS_D$ , (3)

high RMSE values in the higher range of  $TSS_D$ , and (4) low RMSE values in the higher range of  $TSS_D$ . In the first region are BISON runs where hydride precipitates at the cold end solely due to hydride growth. Although low  $TSS_D$  values can drive sufficient amounts of solute hydrogen towards the cold end to initiate the growth of existing hydride, the hydrogen concentration in solution is insufficient to allow the nucleation of new hydrides. Thus, the RMSE linearly increases with increasing  $TSS_D$  like that for specimen A46 in Figure 4. When it comes to the second region,  $TSS_D$  is now large enough to drive more solute hydrogen towards the cold end, enough to exceed  $TSS_P$ , and thus, both the nucleation and the growth of hydride are allowed. Hence, increasing  $TSS_D$  in this region leads to much more precipitations of hydride than in the first region, resulting in a drastic increase of the RMSE as shown in the scatter plots. Finally, the maximum allowable amount of hydrogen is reached and the calculated RMSE is saturated with respect to  $TSS_D$  values like observed in the third region. This hypothesis can be supported by the scatter plot of relative RMSE with respect to  $TSS_D$  with the other parameters fixed, as shown in Figure 7. Note that the fourth region is for runs where no precipitation occurred. Finally, these results reveal the importance of the  $TSS_D$  parameter in the HNGD model when determining the amount of hydride precipitated at the cold end in the case where the temperature is low enough to allow for a nucleation of initially precipitated hydride at the cold end of the specimen.

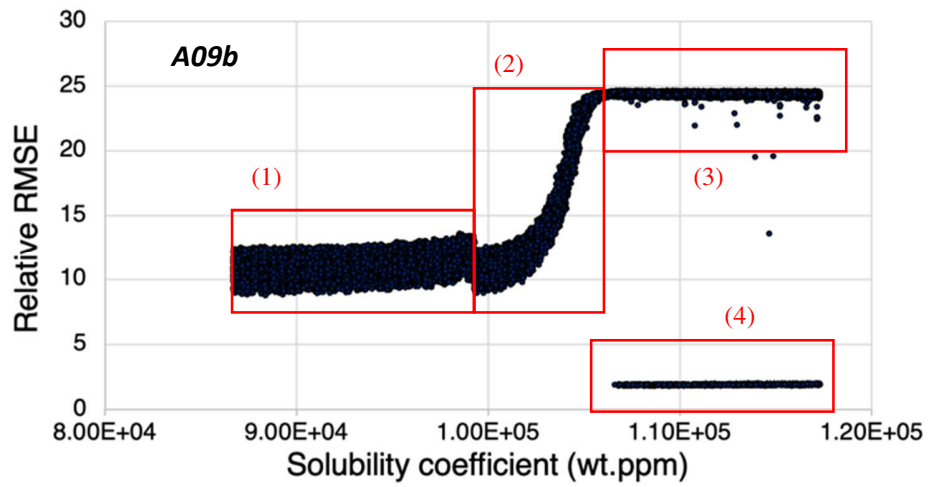


Figure 5. Scatter plot of relative RMSE with respect to the solubility coefficient for specimen A09b.

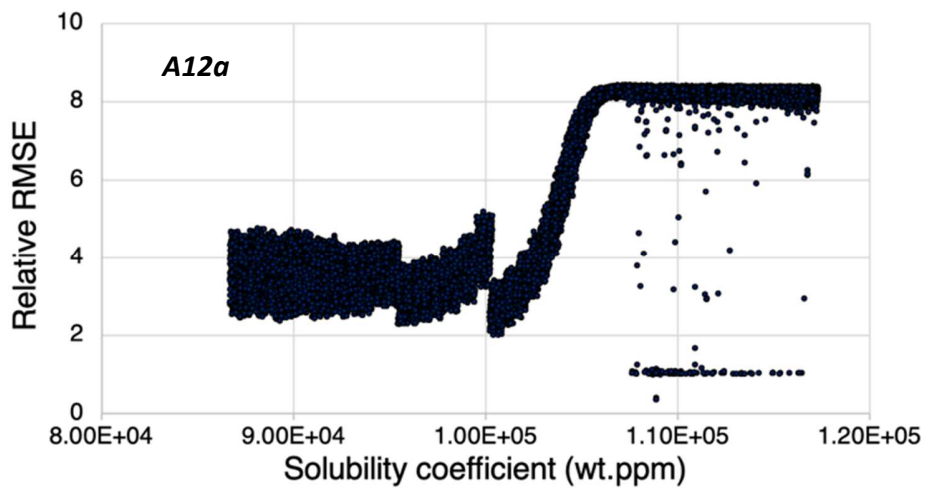


Figure 6. Scatter plot of relative RMSE with respect to the solubility coefficient for specimen A12a.

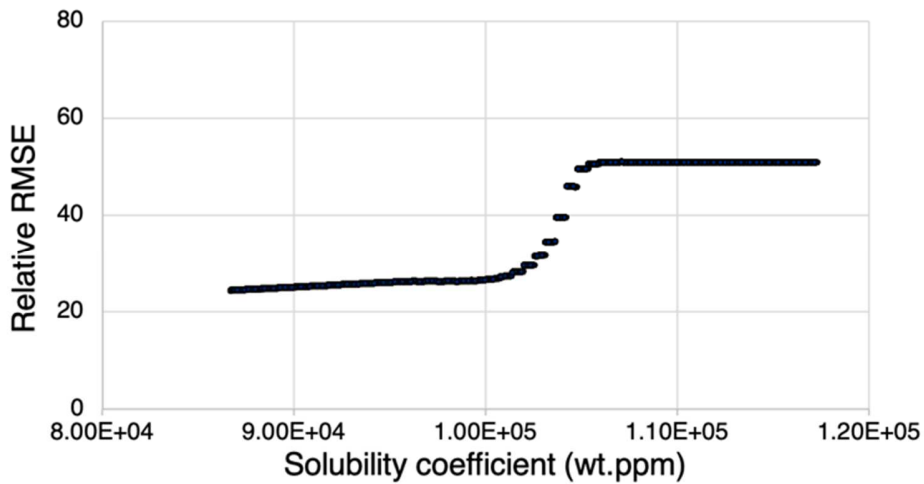


Figure 7. Scatter plot of relative RMSE with respect to the solubility coefficient with the other parameters fixed to arbitrary value.

The scatter plot for specimen A14 shown in Figure 8 presents two separate regions where high RMSEs and low RMSEs are calculated, respectively. As described for specimen A09b and A12a, high RMSE values were calculated in BISON runs where hydride precipitated at the cold end, while BISON runs where no precipitation occurred gave low RMSE values. Note that while some BISON runs predicted hydride precipitation at the cold end, the experimental hydrogen measurements indicate no precipitation occurred for specimen A14 due to its high temperature at the cold end. In the BISON simulations of this specimen, hydride precipitation occurs only at the last node of the specimens, and the large initial hydrogen content of specimen A14 made the calculated hydrogen concentration at the last node to easily exceed  $TSS_D$  or  $TSS_P$ .

The large variability in the RMSE values over the entire range of the solubility coefficient is attributed to the test conditions for specimen A14. Unlike the other specimens, the high temperature condition of specimen A14 allowed all the initial hydride content at the cold end to dissolve. Therefore, the precipitation of hydride was able to initiate only when the concentration of solute hydrogen at the cold end exceeded  $TSS_P$ . BISON simulations that

predicted no precipitation produced low RMSE values as shown at the bottom region of the scatter plot. However, once precipitation was predicted to occur, a large amount of hydride precipitated at the cold end due to both the nucleation and growth models, resulting in high RMSE values.

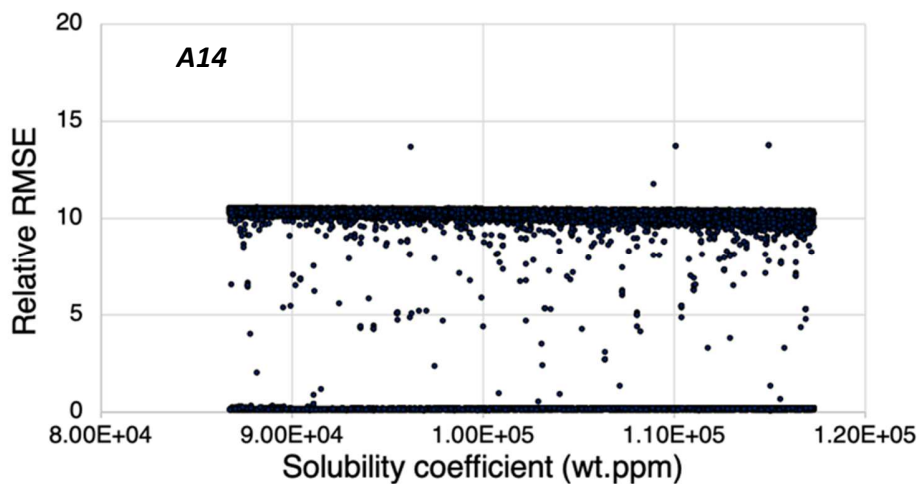


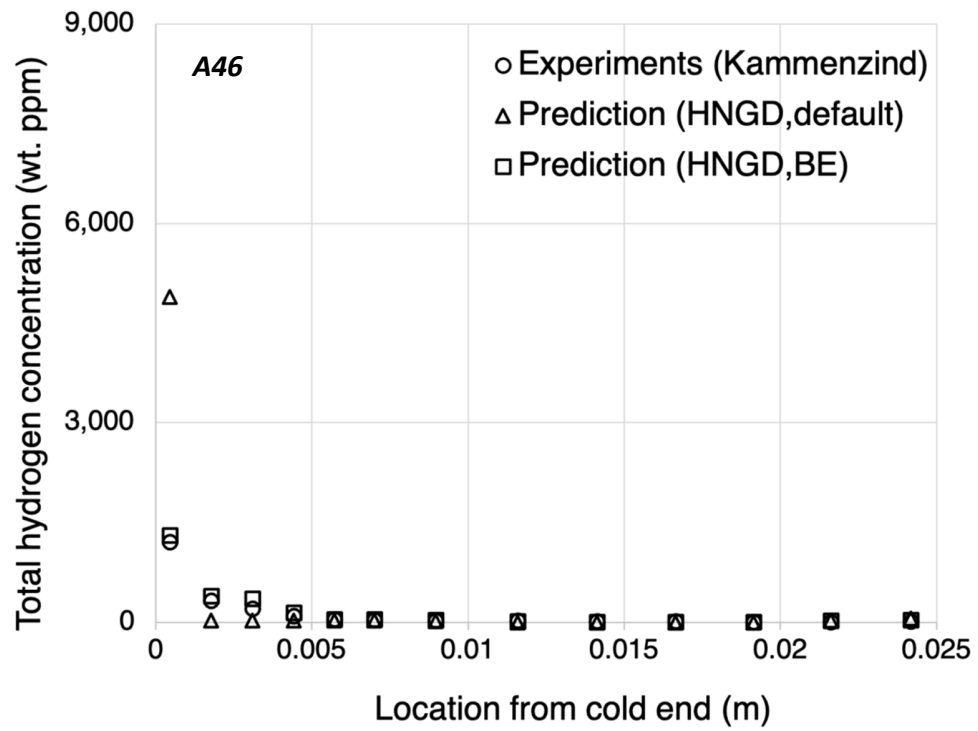
Figure 8. Scatter plot of relative RMSE with respect to the solubility coefficient for specimen A14.

Informed by the results of sensitivity analysis for five specimens, we obtained a calibrated set of parameters listed in Table 3 that provided best-estimate BISON predictions for five specimens. Figure 9(a)-(e) present total hydrogen profiles for specimens estimated by BISON simulations using default values and the calibrated set of parameters. The calibrated set of parameters allowed for better predictions of total hydrogen distribution inside the specimens annealed under linear temperature profile. Specifically, BISON simulations for specimens A46 and A14 showed the best agreement with the measured hydrogen profile. For the specimen A09a, BISON simulation using the calibrated set of parameters estimated smaller hydrogen concentrations than that using default values where 0.26 was calculated for the RMSE. However,

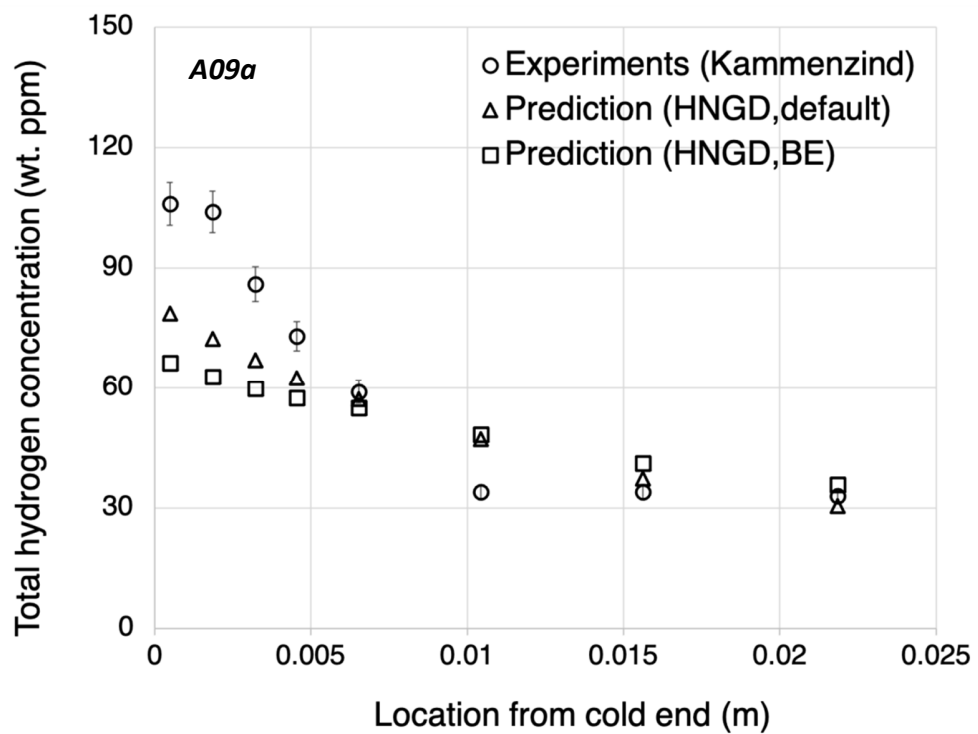
the RMSE computed for the best-estimate simulation was less than 0.4 which still indicated an accurate prediction. Overall, the calibrated set of parameters in HNGD model significantly improved the accuracy of BISON predictions of hydrogen behaviors under various thermal conditions, though the fundamental physics beneath it needs to be further investigated in future work.

Table 3. Calibrated set of parameters for best-estimate predictions of total hydrogen concentration profile.

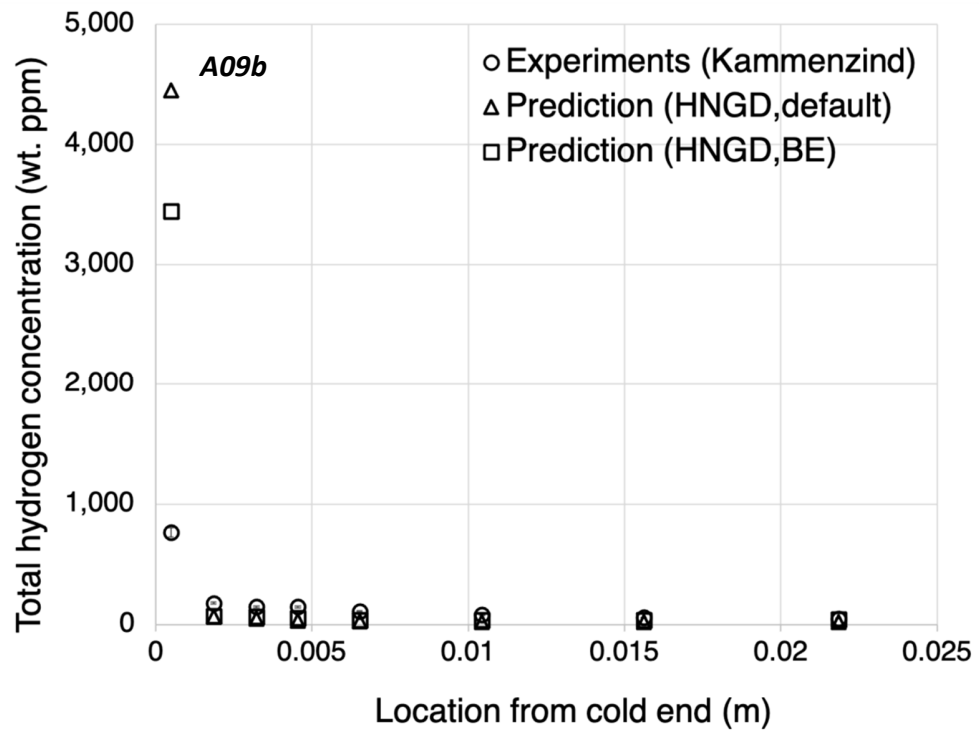
Parameter	Unit	Default	Best-estimate
Heat of transport, $Q^*$	<i>J/mole</i>	26200	18394
Diffusion coefficient: pre-exponential factor, $D_0$	<i>m<sup>2</sup>/s</i>	$7.9 \cdot 10^{-7}$	$6.37 \cdot 10^{-7}$
Supersolubility coefficient (=TSS <sub>P</sub> ), $TSS_{P0}$	<i>wt. ppm</i>	31000	35018
Solubility coefficient (=TSS <sub>D</sub> ), $TSS_{D0}$	<i>wt. ppm</i>	102000	88366
Nucleation kinetic parameter: coefficient, $K_{N0}$	<i>s<sup>-1</sup></i>	$2.75 \cdot 10^{-5}$	$2.81 \cdot 10^{-5}$
Diffusion-controlled growth kinetic parameter: coefficient, $K_{mob0}$	<i>s<sup>-1</sup></i>	55000	52622
Reaction-controlled growth kinetic parameter: coefficient, $K_{th0}$	<i>s<sup>-1</sup></i>	$1.6 \cdot 10^{-5}$	$1.55 \cdot 10^{-5}$
Dissolution kinetic parameter: coefficient, $K_{D0}$	<i>s<sup>-1</sup></i>	4100	4030



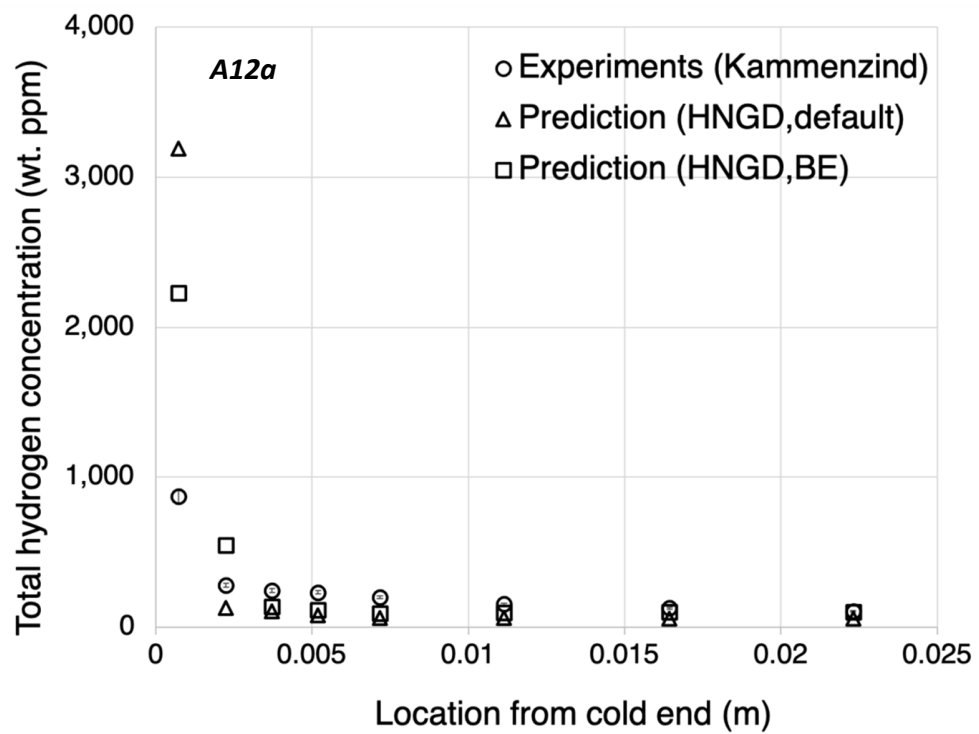
(a)



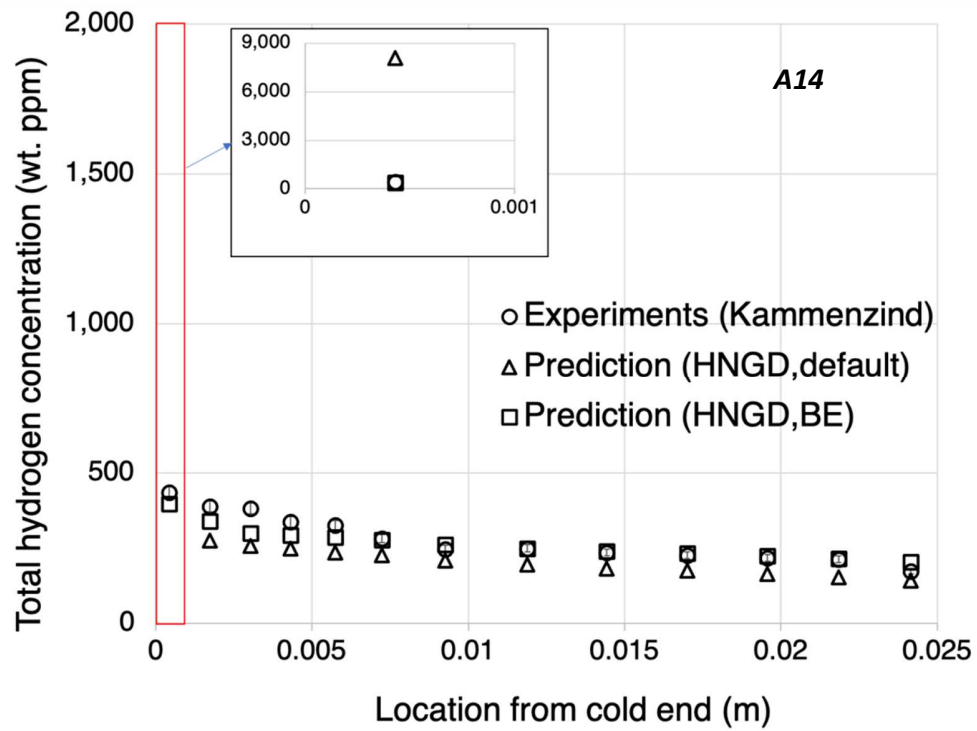
(b)



(c)



(d)



(e)

Figure 9. Best-estimate predictions for specimens annealed under linear temperature profile using calibrated set of parameters: (a) specimen A46, (b) specimen A09a, (c) specimen A09b, (d) specimen A12a, (e) specimen A14.

#### 4.2 Global sensitivity analysis of the HNGD model under asymmetric temperature profiles

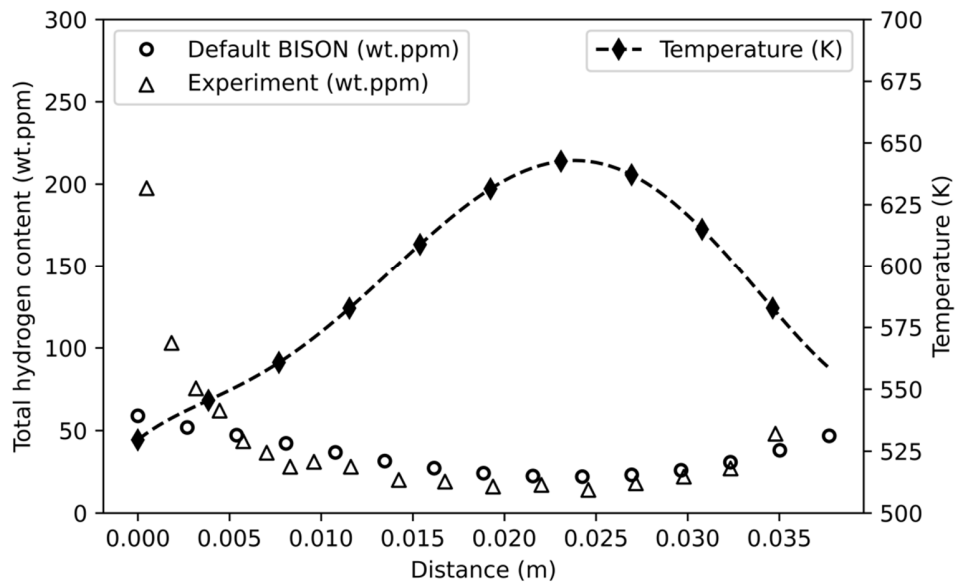
A global sensitivity analysis of the overall accuracy of predicted hydrogen distributions under asymmetric temperature profiles was conducted using the same parametric ranges in Table 1. The BISON simulations and experimental results were compared with a relative RMSE calculation across all measurement locations, excluding the data point that was located at the

hydride rim region. This data point was neglected because of large uncertainties in experimental measurements at this location and the purpose of the hydride rim was only to act as a source of hydrogen throughout the annealing period, to be redistributed throughout the sample. The experimental conditions for the asymmetric cases are listed in Table 4.

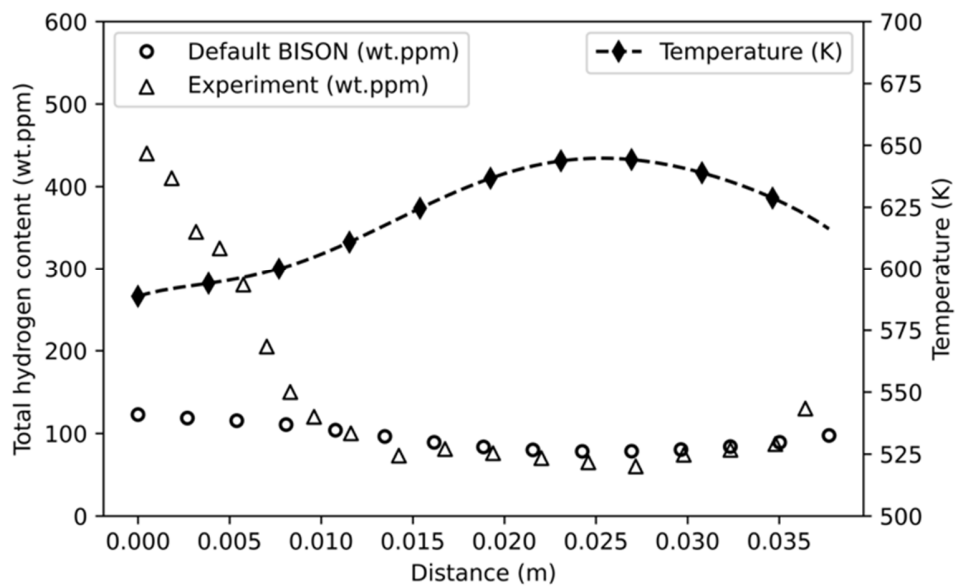
Table 4. Chosen experiments under asymmetric temperature profile from historic data (Kammenzind B. F., et al., 1996; Merlino J. T., 2019)

	<b>Anneal time [day]</b>	<b>Cold end Temp. [K]</b>	<b>Peak Temp. [K]</b>	<b>Hot end Temp. [K]</b>
A53	150	533	644	575
A54	194	533	644	575
A55a	209	589	644	616
A56	95	533	644	575

Default BISON simulations for two of the asymmetric temperature cases are shown in Figure 10 compared with the experimental data. In the simulations, the hydride rim located at the hotter end of the specimens dissolved partially, and supplied solute hydrogen into the rest of the sample throughout the annealing period. The hydrogen in solid solution migrated to the cold side and built up at the cold end. However, due to the low thermal driving force, the predicted concentration of solute hydrogen at the cooler end did not reach  $TSS_P$  to cause hydride nucleation in all of the calculations, thus no precipitation occurred in all BISON simulations. Since hydrides actually did precipitate near the cold end in the experiments, this led to a large discrepancy between predicted and posttest measured hydrogen profiles over the length of the samples. To identify key parameters that contributed to the discrepancy, Sobol indices of respective input parameters were computed.



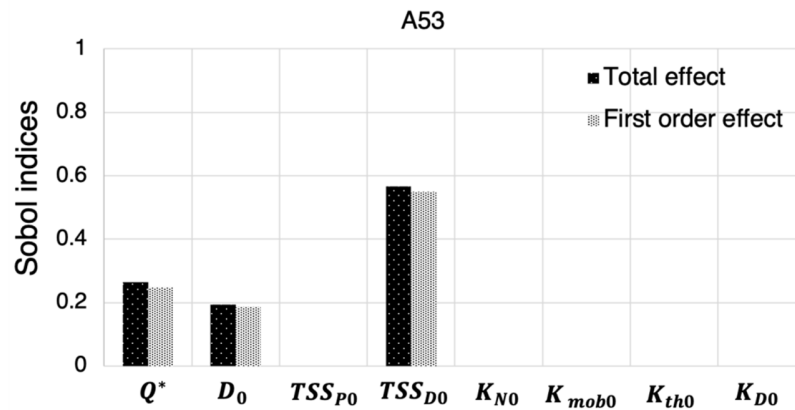
(a)



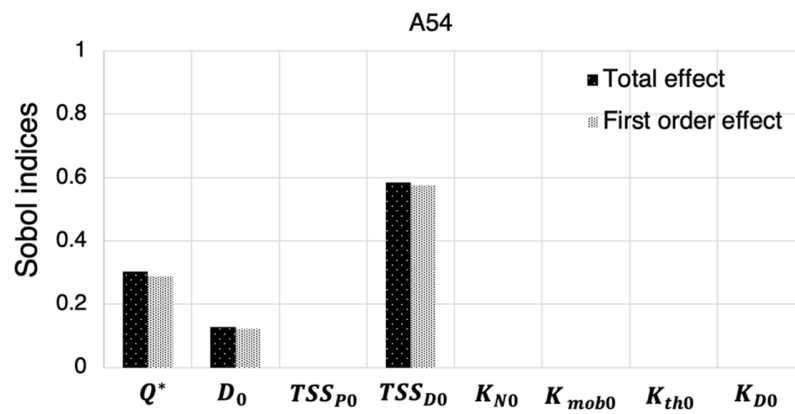
(b)

Figure 10. Default BISON prediction of hydrogen profile, temperature gradient, and posttest measured hydrogen values for asymmetric cases: (a) specimen A53, (b) specimen A55a.

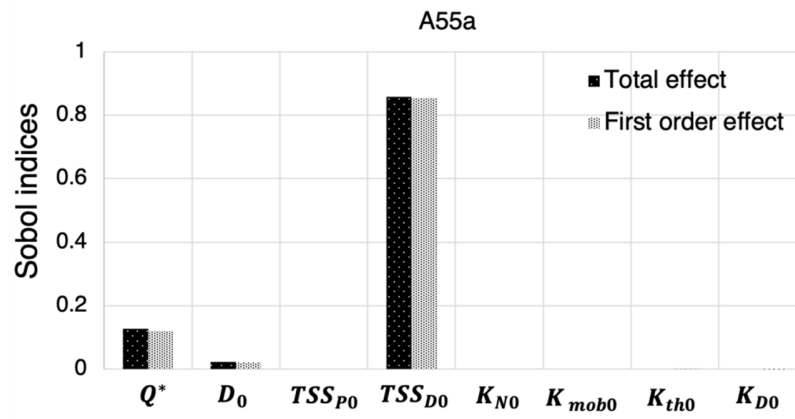
Sobol indices computed for each sample are shown in Figure 11. For all cases, the solubility coefficient gave the largest impact on the predicted hydrogen distribution, followed by the heat of transport and the diffusion coefficient. Because solubility determines the amount of solute hydrogen which dissolves from the hydride rim and migrates towards the cooler end, it gave the largest Sobol indices. Once the dissolved hydrogen in solid solution reaches the location where the temperature is maximum, the hydrogen diffusion towards the left end is enhanced by the Soret effect. This caused large contributions of the heat of transport and the diffusion coefficient to the predicted hydrogen profile. Since there was no predicted hydride precipitated at the cold end, Sobol indices of parameters related to precipitation kinetics as well as  $TSS_P$  were negligible. For specimen A55a, the influence of solubility was much more prevalent than for the other specimens, since the cooler and hotter end temperatures were higher than all the other samples, providing more solute hydrogen that could migrate towards the cooler end.



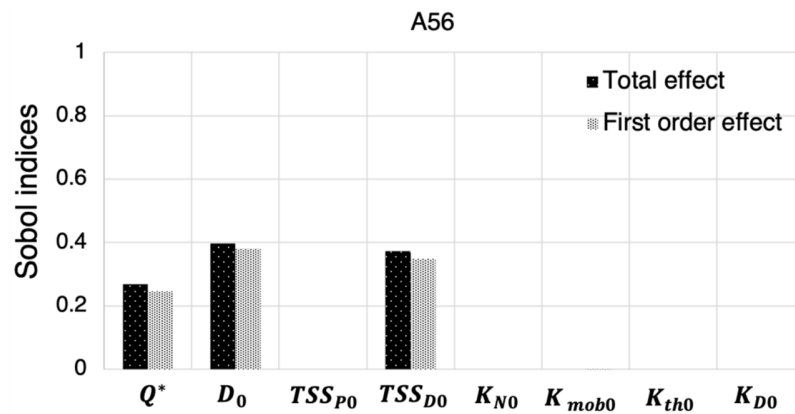
(a)



(b)



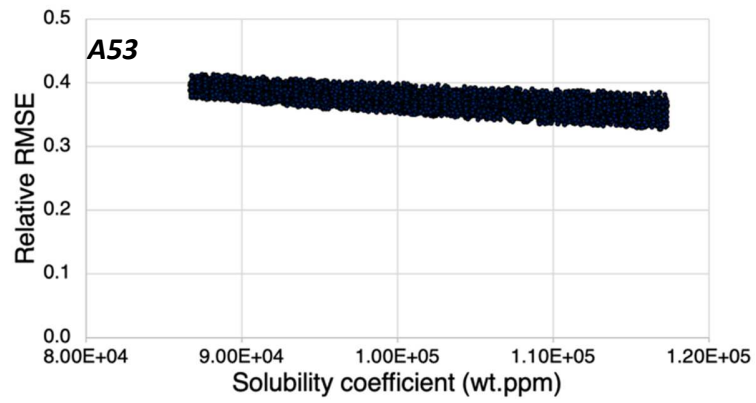
(c)



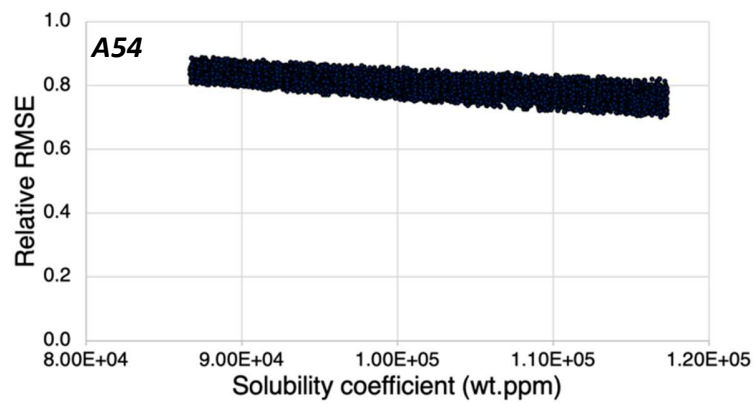
(d)

Figure 11. Sobol indices of input parameters computed from RMSE for asymmetric cases: (a) specimen A53, (b) specimen A54, (c) specimen A55a, (d) specimen A56.

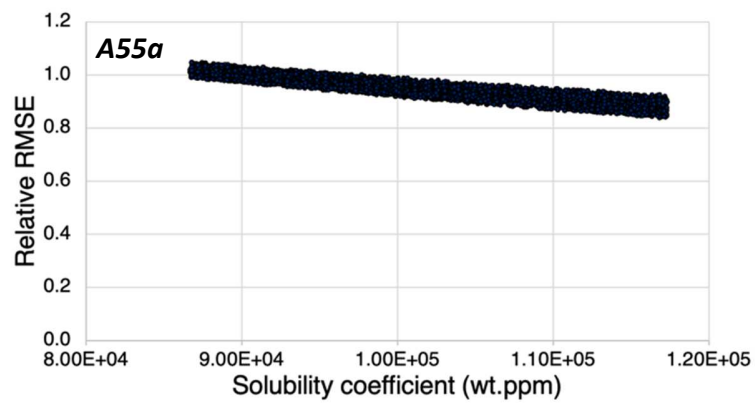
Unlike the linear temperature samples, the asymmetric temperature samples were not uniformly precharged with hydrogen prior to testing. Only a hydride surface rim located at the hotter end of the asymmetric temperature samples was cathodically applied prior to testing. This hydride rim provided a source of hydrogen to flow to the cooler end of the sample over the course of the anneals. Without pre-existing hydride at the cooler end of the sample, precipitation is predicted to occur only when the concentration of solute hydrogen exceeded  $TSS_P$ . Because of the small temperature gradient, the predicted thermally driven hydrogen diffusion did not build enough hydrogen in solid solution at the cooler end to exceed  $TSS_P$ , which led to no predicted hydride precipitation. While this made BISON simulations underpredict the measured posttest hydrogen distribution near the cooler end for all runs, higher solubility coefficients did predict more hydrides to dissolve from the hotter end and provide more solute hydrogen near the cold end. Therefore, the calculated RMSE was reduced as the solubility coefficient increased, as shown in the scatter plots in Figure 12. Within the variation ranges of parameters, any combination of them did not predict the precipitation of hydride, and thus, the calibrated set of parameters obtained in Section 4.1 also did not provide a better agreement with the measured data. Since a large discrepancy in hydrogen distribution between simulations and experiments still existed, BISON simulations need to account for the precipitation of hydride under these asymmetric temperature profile to improve the overall accuracy of hydrogen predictions.



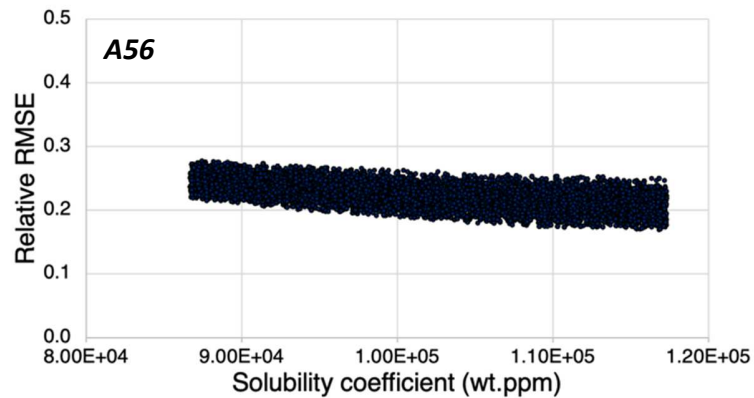
(a)



(b)



(c)



(d)

Figure 12. Scatter plots of calculated RMSE with respect to the solubility coefficient for asymmetric cases: (a) specimen A53, (b) specimen A54, (c) specimen A55a, (d) specimen A56.

#### 4.3 Comparison study between the former BISON model and the HNGD model

The differing methods of calculating hydrogen precipitation between the former BISON model and the HNGD model play an important role in the prediction of hydrogen. Figure 13 is a comparison of the former version of the BISON model with the HNGD model for sample A09b, utilizing same model parameter values. Both models predicted substantial amount of precipitated hydride at the cold end, though the HNGD model estimated much larger hydrides than the former version of BISON model. This is attributed to the difference in precipitation mechanism between two models, as the growth of existing hydride allows for more hydrogen in solid solution to easily precipitate. To characterize the impact of the HNGD model on the predicted hydrogen distribution, scatter plots of predicted hydrogen with respect to  $TSS_P$  and  $TSS_D$  from sensitivity analysis using the former BISON model and the HNGD model were compared for both the linear and asymmetric temperature cases. Because both models utilized different parameters and ranges to account for the hydrogen precipitation and dissolution kinetics, the

present work compares only the tendencies of the output between the two models, and analyzes the difference in possible mechanisms. BISON simulations using the former version of the model employed parameters and their ranges set in previous work (Seo, et al., 2021), while HNGD simulations used parameters and their ranges in Table 1. In addition, as the precipitation of hydride was likely to occur at the cold end, the comparison study presented here focused on the predicted hydrogen concentration at the cold end rather than a calculated RMSE.

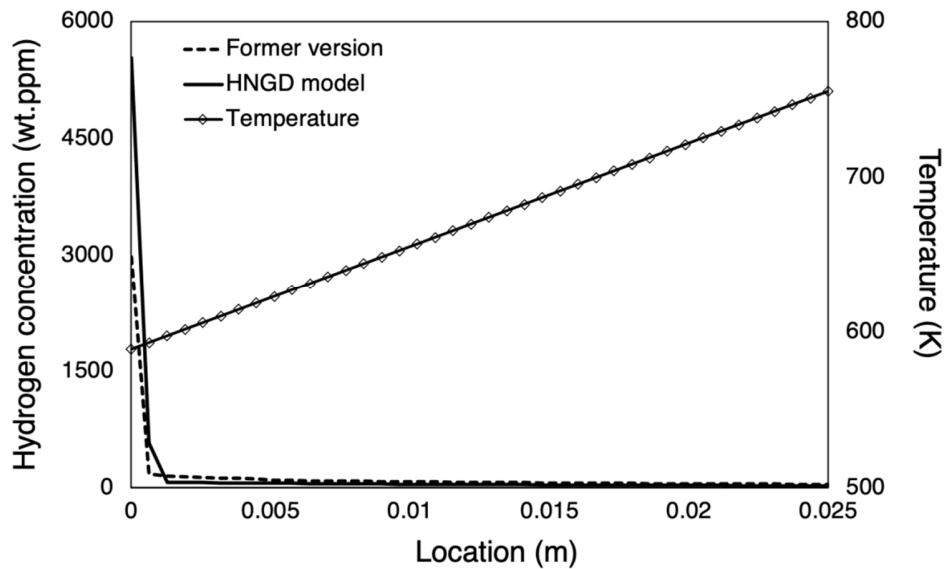
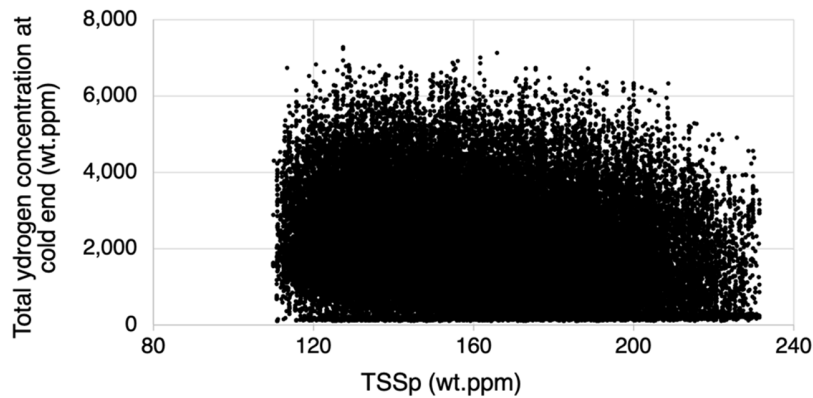


Figure 13. Hydrogen distribution for specimen A09b computed by the former version of BISON model and the HNGD model.

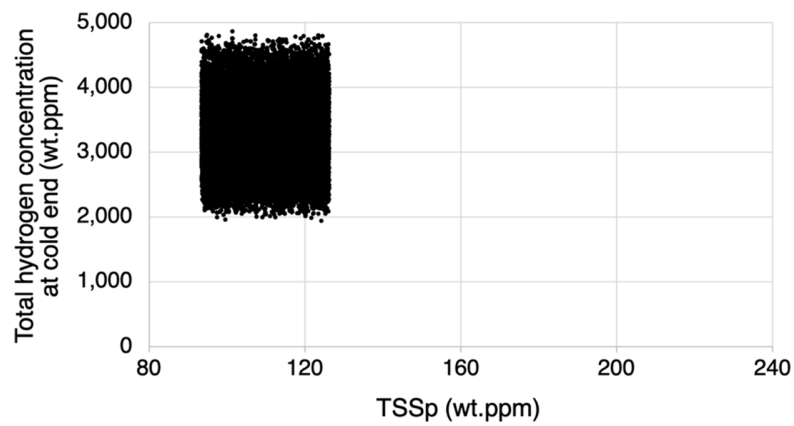
#### 4.3.1 Comparison study for linear temperature case

Figure 14 presents scatter plots of hydrogen concentration at the cold end with respect to  $TSS_P$ , predicted for specimen A46 using the former BISON model and the HNGD model. Note that we plotted the scatters of predicted hydrogen concentration in Figure 14-16 with respect to

the values of  $TSS_P$  and  $TSS_D$ , not the pre-exponential factor or activation energy. This allows for easily understanding of what would be the threshold for the precipitation driven by either nucleation of new hydride when hydrogen concentration in solid solution exceeds  $TSS_P$  value or growth of existing hydride when exceeding  $TSS_D$  value. The predicted hydrogen concentration at the cold end was insensitive to increasing  $TSS_P$  for both models, while the variation of the prediction was much larger for simulations using the former BISON model. The large variation of scatter in Figure 14(a) indicates that some BISON runs using the former model predicted no precipitation of hydride at the cold end, which therefore computed low concentrations of hydrogen. On the other hand, the minimum predicted hydrogen concentration in Figure 14(b) is found to be about 2,000 wt.ppm, which indicates all BISON runs using the HNGD model predicted precipitation of hydride at the cold end for specimen A46. This difference in prediction of precipitation attributes to the hydride growth mechanism, which is the most distinct feature of the HNGD model. For specimen A46, the initially charged hydride near the cold end wasn't fully dissolved at the start of testing due to the low  $TSS_D$  there. As a result, the hydride growth mechanism in the HNGD model allowed precipitation to occur in every run, in areas with existing hydrides and where the concentration of solute hydrogen exceeded  $TSS_D$ , even though the concentration of hydrogen in solid solution did not exceed  $TSS_P$ . However, in the former version of the BISON model, hydride was able to precipitate only when the concentration of solute hydrogen exceeded  $TSS_P$ , regardless of the existence of hydride, hence some runs did not predict any precipitation at the cold end.



(a)

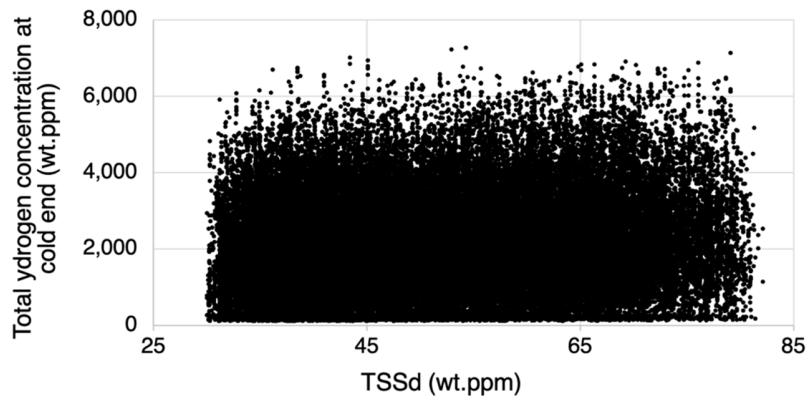


(b)

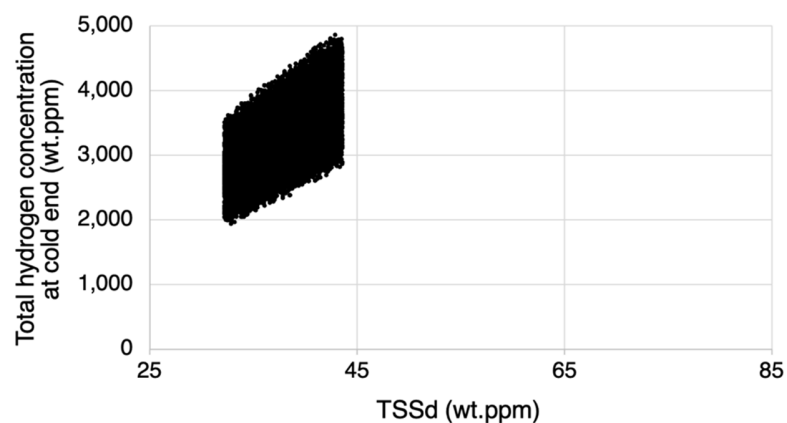
Figure 14. Scatter plots of predicted hydrogen with respect to  $TSS_P$  for specimen A46: (a) using the former BISON model, (b) using the HNGD model.

Scatter plots of predicted hydrogen concentration at the cold end of Specimen A46 with respect to  $TSS_D$ , shown in Figure 15, verified the significant impact of the hydride growth mechanism on the predicted cold end hydrogen concentration. The concentration of total hydrogen at the cold end predicted by the former BISON model showed little sensitivity to changes in  $TSS_D$ , whereas scatter plots predicted by the HNGD model presented a linear correlation in the total amount of hydrogen at the cold end to the  $TSS_D$  value. More hydride was predicted to precipitate at the cold end as  $TSS_D$  increased, because of the larger driving force for

dissolution from the hotter regions of the specimen, as described in Section 4.1. As stated, hydrides precipitated in every BISON run using the HNGD model for specimen A46. In such a situation, the amount of solute hydrogen migrating from neighboring locations could directly determine the amount of hydride precipitated at the cold end, and  $TSS_D$  is the parameter which estimates the possible concentration of hydrogen in solid solution near the cold end. This led to a clear and linear correlation between the predicted hydrogen concentration and  $TSS_D$  values, as shown in Figure 15(b).



(a)



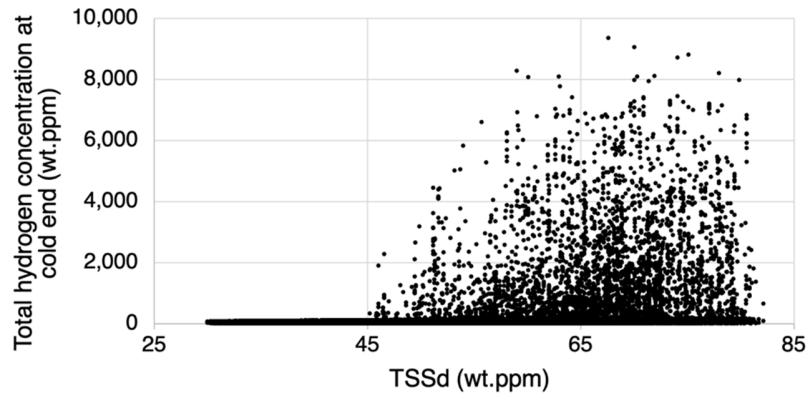
(b)

Figure 15. Scatter plots of predicted hydrogen with respect to  $TSS_D$  for specimen A46: (a) using the former BISON model, (b) using the HNGD model.

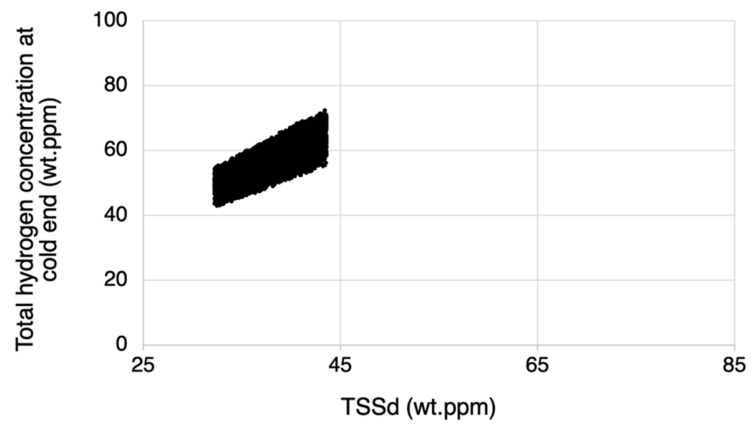
#### 4.3.2 Comparison study for asymmetric temperature case

Figure 16 are scatter plots of the computed total hydrogen concentration as a function of  $TSS_d$  at the cold end for an asymmetric temperature profile, specimen A53, for the (a) former model of BISON and parameter range and (b) HNGD model of BISON and parameter range. The dissolution of the hydride rim greatly influences the amount of hydrogen that is able to migrate to the other end of the sample. The former model of BISON and its parameter range allows for enough hydrogen in solid solution at the cold end to precipitate cold end. Where precipitation does not occur, when  $TSS_D$  is low, both models predict the concentration of hydrogen at the cold end similarly. It is to be noted that  $TSS_D$  was not varied to as high a level in the HNGD model as it was in the former BISON model.

For both models, increasing  $TSS_D$  allowed for more solute hydrogen to dissolve from the hydride rim and thus more hydrogen could be built up at the cold end. However, without any existing hydride, both models predicted no precipitation of hydride to occur in the low range of  $TSS_D$  values. In other words, the two models gave no significant difference in predicting hydrogen distribution when hydride did not precipitate. Along with the results for the linear temperature cases, it is concluded that the existence of initial hydride gives a significant impact on the predicted hydrogen concentration by the HNGD model; larger than that by the former BISON model due to the hydride growth mechanism. And thus, the accuracy of the HNGD model is more sensitive to the environmental conditions such as temperature or initial state of the sample that can determine the existence of initial hydride.



(a)



(b)

Figure 16. Scatter plots of predicted hydrogen with respect to TSS<sub>D</sub> for specimen A53: (a) using the former BISON model, (b) using the HNGD model.

## 5. Conclusion

The Hydride Nucleation-Growth-Dissolution (HNGD) model was implemented into the BISON code to account for hydride formation throughout the cladding. This paper presents a sensitivity analysis of the HNGD model aiming to quantify impacts on the prediction of hydrogen behavior under various environmental conditions. This includes identifying the key parameters in the HNGD model under different environmental conditions, quantifying the impact of an improved model on the prediction of hydrogen, and revealing the significant impact of the newly-implemented phenomena by comparison with the former model in BISON. The relative Root Mean Square Error (RMSE) from the BISON predictions to the actual experiments is chosen as the operating Figure of Merit (FoM), and the set of input parameters includes model parameters related to the HNGD model. Global sensitivity analyses employing a Sobol technique compute sensitivity measures and scatter plots for various experimental cases subjected to linear temperature profiles and asymmetric temperature profiles.

Under linear temperature profiles with initially uniformly distributed hydrogen concentrations, BISON simulations using the HNGD model give two distinct results. The heat of transport dominates the accuracy of prediction in cases where no precipitation occurs at the cold end, while  $TSS_D$  is the most important parameter when precipitation occurs. Somewhat counterintuitively, higher  $TSS_D$  leads to more precipitation of hydrides at the cold end, even though the concentration of hydrogen in solid solution increases as  $TSS_D$  increases. Of course, no growth of existing hydrides is eventually predicted when  $TSS_D$  becomes much higher. This results in a large variation in predicted hydrogen concentration between BISON runs with or without precipitation.

Under asymmetric temperature conditions with an initial hydride rim precharged at the specimen hotter end, solubility coefficients give the largest impacts on the predicted hydrogen distribution, followed by heat of transport, and the diffusion coefficient. For all BISON runs, the low thermal diffusion driving force in the asymmetric samples does not allow for sufficient hydrogen to build in solid solution at the cooler end to initiate the nucleation of hydride. However, precipitation actually occurred in the experiments. Since BISON simulations fail to predict precipitation of hydride in these samples, a large discrepancy in hydrogen distribution between simulations and experiments exists, which need to be accounted for in order to improve the overall accuracy of the model.

Comparative studies using the former and updated models verifies the significant impact of the hydride growth mechanism on predicted hydride formation and hydrogen accumulation under an imposed temperature gradient. The concentration of hydrogen predicted by the former BISON model is insensitive to  $TSS_D$  values, whereas that predicted by the HNGD model is positively correlated with them. In particular, when hydride initially exists, changes in  $TSS_D$  generate a large variation in the predicted amount of precipitation by hydride growth, giving large uncertainty in predicting hydrogen distribution over the sample.

Overall, two primary issues were seen in these studies, benchmarking the BISON model to thermal migration experiments. First the HNGD model in BISON code using the default parameters for  $TSS_D$  and  $TSS_P$  do not predict precipitation in several instances, when precipitation actually did occur. Second, the BISON model overpredicts the segregation of hydride precipitation to the coldest nodes in the finite element mesh, when the experimental results show the hydride precipitation to be more spread out, even extending up the temperature gradient some. Recent study by Passelaigue et al. (Passelaigue, Simon, & Motta, 2022)

introduced a physical model into the HNGD model with new parameters, and reported the improvement in predictions of hydrogen distribution under linear and asymmetric temperature profiles. We expect the future work planning to validate the modified HNGD model against separate-effect experiments may fully resolve the issues.

## **Acknowledgement**

This work was funded by a U.S. Department of Energy Integrated Research Project entitled “Development of a Mechanistic Hydride Behavior Model for Spent Fuel Cladding Storage and Transportation: IRP-FC-1: Modeling of Spent Fuel Cladding in Storage and Transportation Environments”. This research made use of the resources of the High Performance Computing Center at Idaho National Laboratory, which is supported by the Office of Nuclear Energy of the U.S. Department of Energy and the Nuclear Science User Facilities under Contract No. DE-AC07-05ID14517. We gratefully thank Dr. Albert Casagrande, Dr. Giovanni Pastore, and Florian Passelaigue for helping us build and run BISON simulations. We appreciate Miles O’Neal for his contribution in preparing manuscript.

## REFERENCES

- A. Tanweer, et al. (2011). A review on the clad failure studies. *Nuclear Engineering and Design*, 241(9), 3658-3677.
- Aly Z., et al. (2019). Aly, Z., Casagrande, A., Pastore, G., & Brown, N. R. (2019). Variance-based sensitivity analysis applied to hydrogen migration and redistribution model in Bison. Part I: Simulation of historical experiments. *Journal of Nuclear Materials*(524), 20-100.
- Aly Z., et al. (2019). Variance-based sensitivity analysis applied to the hydrogen migration and redistribution model in Bison. Part II: Uncertainty quantification and optimization. *Journal of Nuclear Materials*(523), 478-489.
- Arsene S., et al. (2003). Hydride embrittlement and irradiation effects on the hoop mechanical properties of pressurized water reactor (PWR) and boiling-water reactor (BWR) zircaloy cladding tubes: part I. hydride embrittlement in stress-relieved, annealed, and recrystallized zirc. *Metallurgical and Materials Transactions A*, 3(34), 553-566.
- Asher, R. C., and F. W. Trowse. (1970). The distribution of hydrogen in zirconium alloy fuel cladding: The effects of heat flux. *Journal of Nuclear Materials*(35.1), 115-121.
- Bruni, G., Lewis, B., & Thompson, W. (2010). Framework model for hydrogen redistribution in Zircaloy sheathing. *Journal of Nuclear Materials*, 409(1), 33-39.
- Colas, K., Motta, A. T., Daymond, M. R., & Almer, J. D. (2014). Mechanisms of hydride reorientation in Zircaloy-4 studied in situ. *Zirconium in the Nuclear Industry: 17th International Symposium, ASTM STP 1543*, 1107–1137.
- Courty, O. et al. (2014). Modeling and simulation of hydrogen behavior in Zircaloy-4 fuel cladding. *Journal of Nuclear Materials*(452), 311-320.
- Ells C. E. (1968). hydride precipitates in zirconium alloys. *Journal of Nuclear Materials*(28), 129-151.
- Hamamoto, Y., Uchikoshi, T., & Tanabe, K. (2020). Comprehensive Modeling of Hydrogen Transport and Accumulation in Titanium and Zirconium. *Nuclear Materials and Energy*, 23, 100751.
- Herman J. and Usher W. (2017). SALib: an open-source Python library for sensitivity analysis. *Journal of Open Source Software* (97).
- Kammenzind B. F., et al. (1996). Hydrogen pickup and redistribution in alpha-annealed Zircaloy-4. *ASTM STP 1295 Zirconium in the Nuclear Industry: 11th International Symposium*, 338-370.
- Kolesnik, M., Aliev, T., & Likhanskii, V. (2018). Modeling of hydrogen behavior in spent fuel claddings during dry storage. *Journal of Nuclear Materials*, 508, 567-573.
- Lacroix E. et al. (2021). Zirconium hydride precipitation and dissolution kinetics in the hysteresis region in zirconium alloys. *Zirconium in the Nuclear Industry: 19th International Symposium, STP 1622*.
- Lacroix, E., Motta, A. T., & Almer, J. D. (2018). Experimental determination of zirconium hydride precipitation and dissolution in zirconium alloy. *Journal of Nuclear Materials*, 509, 162-167.
- McMinn, A., Darby, E. C., & Schofield, J. S. (2000). The terminal solid solubility of hydrogen in zirconium alloys. *Zirconium in the Nuclear Industry: Twelfth International Symposium, ASTM STP 1354*, 173–195.

- Merlino J. T. (2019). EXPERIMENTS IN HYDROGEN DISTRIBUTION IN THERMAL GRADIENTS CALCULATED USING BISON. *Masters paper in Nuclear Engineering*. The Pennsylvania State University.
- Motta A. T., et al. (2019). Hydrogen in zirconium alloys: A review. *Journal of Nuclear Materials*(518), 440-460.
- Passelaigue F. et al. (2021). Implementation and Validation of the Hydride Nucleation-Growth-Dissolution (HNGD) model in BISON. *Journal of Nuclear Materials*, 544.
- Passelaigue, F., Simon, P.-C. A., & Motta, A. T. (2022). Predicting the hydride rim by improving the solubility limits in the Hydride Nucleation-Growth-Dissolution (HNGD) model. *Journal of Nuclear Materials*, 153363.
- Puls, M. (2012). *The Effect of Hydrogen and Hydrides on the Integrity of Zirconium Alloy Components: Delayed Hydride Cracking*. London: Springer.
- Richmond D. J. and Geelhood K. J. (2018). FRAPCON analysis of cladding performance during dry storage operations. *Nuclear Engineering and Technology*, 50(2), 306-312.
- Saltelli A. (2002). Making best use of model evaluations to compute sensitivity indices. *Computer Physics Communications*, 145(2), 280-297.
- Saltelli A. et al. (2010). Variance based sensitivity analysis of model output. Design and estimator for the total sensitivity index. *Computer Physics Communications*, 181(2), 259-270.
- Sarrazin F. et al. (2016). Global Sensitivity Analysis of environmental models: Convergence and validation. *Environmental Modelling & Software*, 79, 135-152.
- Seo, S., Duchnowski, E. M., O'Neal, M., Motta, A. T., Passelaigue, F., Kang, S., . . . Brown, N. R. (2021). Sensitivity Analysis of BISON Model for Characterization of Impact of Experimental Parameters on Hydrogen Migration and Redistribution in Zirconium-based Alloys. *Journal of Nuclear Materials*, 550, 152941.
- Sobol I. (1993). Sensitivity Estimates for Non Linear Mathematical Models. *Mathematical Modelling and Computational Experiment*, 1, 407-414.
- Stafford, D. S. (2015). Multidimensional simulations of hydrides during fuel rod lifecycle. *Journal of Nuclear Materials*, 466, 362-371.
- Une, K., & Ishimoto, S. (2003). Dissolution and precipitation behavior of hydrides in Zircaloy-2 and high Fe Zircaloy. *Journal of Nuclear Materials*, 322, 66-72.
- Williamson R. L., et al. (2012). Multidimensional multiphysics simulation of nuclear fuel behavior. *Journal of Nuclear Materials*, 423(1-3), 149-163.